PRediction Of Geospace Radiation Environment and Solar wind parameterS

Work Package 4
Development of new statistical wave models and the re-estimation of the quasilinear diffusion coefficients.

Deliverable 4.2
Report describing the database of emissions occurrences

Vitalii Shastun, Vladimir Krasnoselskikh, Oleksiy Agapitov, Michael Balikhin, Simon Walker, Richard Boynton

February 28th, 2016

This project has received funding from the *European Unions Horizon 2020 research and innovation programme* under grant agreement No 637302.

Document Change Record

Issue	Date	Author	Details
1.0			Initial draft
2.0	2015-02-28	SNW/MAB	Rewrite

Contents

Summary

The deliverable D4.2 entitled "Report describing the database of emissions occurrences" is the second deliverable of WP4 "Development of the new statistical wave models and the re-estimation of quasilinear diffusion coefficients". The main goal of this WP is to redevelop statistical wave models for whistler mode Chorus, hiss and equatorial magnetosonic waves, that are parameterised by geomagnetic index (K_p, A_E), solar wind velocity and density and accounts for the previous evolution these parameters.

For this database deliverable, 5 spacecraft missions were selected (DE-1, CRRES, Polar, Cluster, THEMIS), which covered most of the key regions of the magnetosphere: the dayside magnetospheric boundary, both at mid-latitudes and in the cusp, the near-Earth magnetospheric tail. We performed automatic detection of Chorus, hiss, and EMW to identify occurrences of the corresponding emission. The database that contains sufficient number of emission occurrences for reliable application of Error Reduction Analysis was created. For each emission type the database is organised by location that contains the wave amplitude and time of their occurrence. Wave emission events were augmented with solar wind data sets freely available from NASA Omniweb, geomagnetic indices (K_p, Dst, A_E) from the World Data Centre for geomagnetism in Kyoto.

In addition, during the development of the database it became obvious that an additional study to ensure the statistical independence of data for the ERR analysis was required, in particular in relation to chorus emissions. To be treated as independent the intersatellite separation distance should exceed the coherency length. Therefore a study of the coherency length was performed for Chorus emissions. This problem does not arise in the case of hiss emissions due to their stochastic nature.

1 Introduction

Understanding the formation, dynamics, and loss of particles in the Earth's radiation belts is a problem that has been studied for decades and that remains incomplete. The

Van Allen radiation belt particle populations exist in a dynamic equilibrium between losses (mainly due to particle precipitation to the upper atmosphere) and re-filling due to external injections, transport and acceleration processes. The recent results from the Van Allen Probes support the local nature of particle acceleration (Reeves *et al.*, 2013), and it is now generally agreed that in-situ acceleration (and scattering) mechanisms are important to the outer radiation belt particles dynamics.

A favoured candidate for driving in-situ acceleration (as well as pitch angle scattering) is the interaction between whistler waves and electrons. Whistlers in the magnetosphere manifest themselves as electromagnetic perturbations generated near the geomagnetic equator and called chorus (structured, coherent, wave packets, the most intense natural electromagnetic emissions in the magnetosphere) and hiss (diffusive, wide band emissions with randomised phases). The maximum chorus wave amplitudes are located in the core of the outer Van Allen radiation belt (Agapitov *et al.*, 2013). This fact, as well as the closeness of their frequency to the electron cyclotron frequency, make them one of the key factors that control the dynamics of the outer radiation belt (Agapitov *et al.*, 2013; Horne *et al.*, 2005; Thorne, 2010).

Development of physical models for particle pitch angle and energy diffusion in the outer radiation belt requires knowledge of quasilinear diffusion coefficients related to the wave-particle interaction processes. In order to estimate the pitch angle diffusion coefficients it is necessary to know distributions of the intensity of whistler waves within outer radiation belts and their polarisation characteristics. At present, models for chorus wave modes are organised by current geomagnetic indices (K_p or A_E) (Agapitov *et al.*, 2013; Horne *et al.*, 2013; Meredith *et al.*, 2012). This organisation assumes that wave occurrence depends only upon current state of the magnetosphere and is independent of the evolution of the magnetosphere. Since the occurrence of waves does can depend on previous states of the magnetosphere and the dependence of wave occurrence on solar wind parameters can be significantly nonlinear adequate wave models should be developed using nonlinear

Mission	Dates	Instrument	Coverage		Spectral coverage
			λ	L	
DE-1	1981-1984	PWI SFR	$< 20°$	2-8	$< 410kHz$
Polar	1996-1997	PWI SFR	$< 90°$	> 2	$< 800kHz$
CRRES	1990-1991	PWE SFR	$< 15°$	2-8	$< 400kHz$
THEMIS 3 s/c	2008-2014	SCM FBK	$< 20°$	2-8	$< 4kHz$
Cluster 4s/c	2001-2010	STAFF	$< 45°$	3-5	$< 4kHz$

Table 1: The set of spacecraft missions used to construct the database

correlation analysis.

The Error Reduction Ratio methodology is a generalisation of correlation analysis that may be applied to nonlinear systems and in a frame of the proposed project it is planned to be used to generate more realistic models that better account for the dynamical processes in the radiation belts, which will potentially lead to more reliable forecasts from first principles based tools. However, application of the ERR approach requires significant amounts of data. Previous experience has shown that the reliable application of this methodology requires data from 1000 or at least 800-900) independent observations (measurements).

2 THEMIS FBK data description

2.1 THEMIS spacecraft

THEMIS consists of five identically-instrumented spacecraft, launched on February 17, 2007. The main goal of this mission is to conduct multi-point investigations of the sub-storm phenomena in the tail of the terrestrial magnetosphere. Orbit parameters are: perigee 470 km; apogee 87330km; period 1870 min, inclination 16°. Spin-stabilized THEMIS probes carry the comprehensive packages of plasma and field instruments needed to determine the cause of geomagnetic substorms. Electric and magnetic fields are observed by three types of sensors on THEMIS. The FGM (Auster *et al.*, 2009) and Search-

Coil Magnetometer (SCM) (Roux *et al.*, 2009) measure the magnetic fields, while the Electric Fields Instrument (EFI) (Bonnell *et al.*, 2008) measures electric fields. The THEMIS search coil magnetometer filter bank (FBK) data are meant for survey-type monitoring of wave power. FBK mode measurements of spectral power of the magnetic field wave activity are made are summarised in table 2.

2.2 THEMIS data availability

The coverage by THEMIS measurements during 2008-2014 is shown in figures 1 and 2 by years and below full covering during all time period is shown in figure 3. The colour coding represents number of measurements spacecraft made in a particular spatial sector during 2008-2014. The left-hand panel shows the orbital coverage in L-shell/λ coordinates which is obtained by summation over all MLT values, while the right-hand panel represents the coverage in L-shell/MLT coordinates obtained by summation over all latitudes along particular L-shell. It can clearly be seen that there is a vast amount of data that is available to be analysed, comprehensively covering all MLT and L-shell in the range 2-8 almost for all levels of geomagnetic activity $0 < K_p < 7$. As geomagnetic activity increases, the data coverage reduces considerable due to the rarity of such periods. The good covering of the low latitude region of the inner magnetosphere give the opportunity to make the VLF/ELF emission data base and to study their properties during different magnetosphere activity conditions during 2008-2014.

All data were divided in to three groups that correspond to different levels of geomagnetic activity: low $0 < K_p < 3$, medium $3 < K_p < 5$ and high activity levels. Distribution of measurements number available for each level of geomagnetic activity are shown on figure 5.

2.3 THEMIS database description

The database contains measurements of lower band chorus, hiss and magnetic sound events of three THEMIS spacecrafts (THA, THD, THE) during 2008-2014. Database

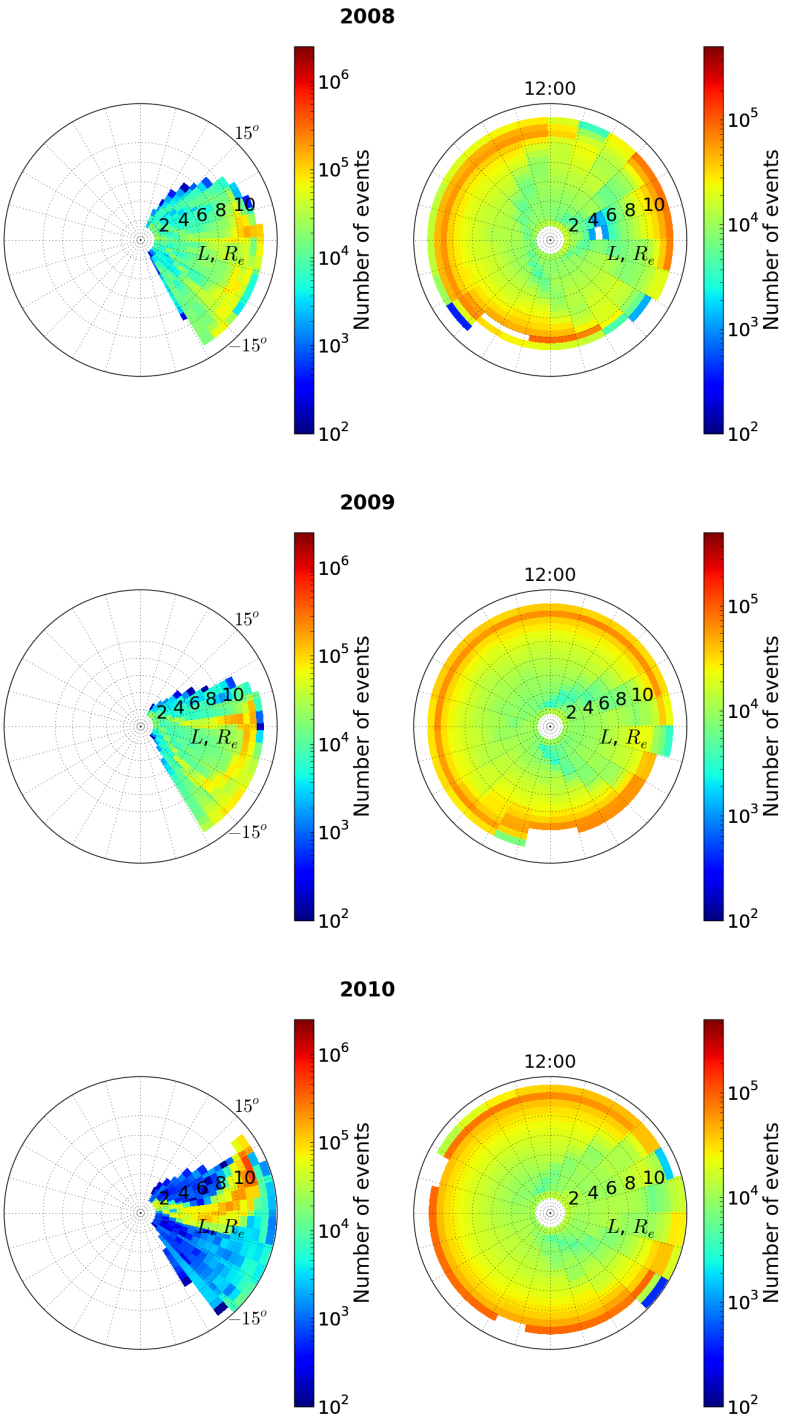

Figure 1: The orbital coverage of THEMIS spacecraft during 2008-2010 within above-specified region by years. The colour coding represents amount of measurements made by the spacecraft in a particular spatial sector.

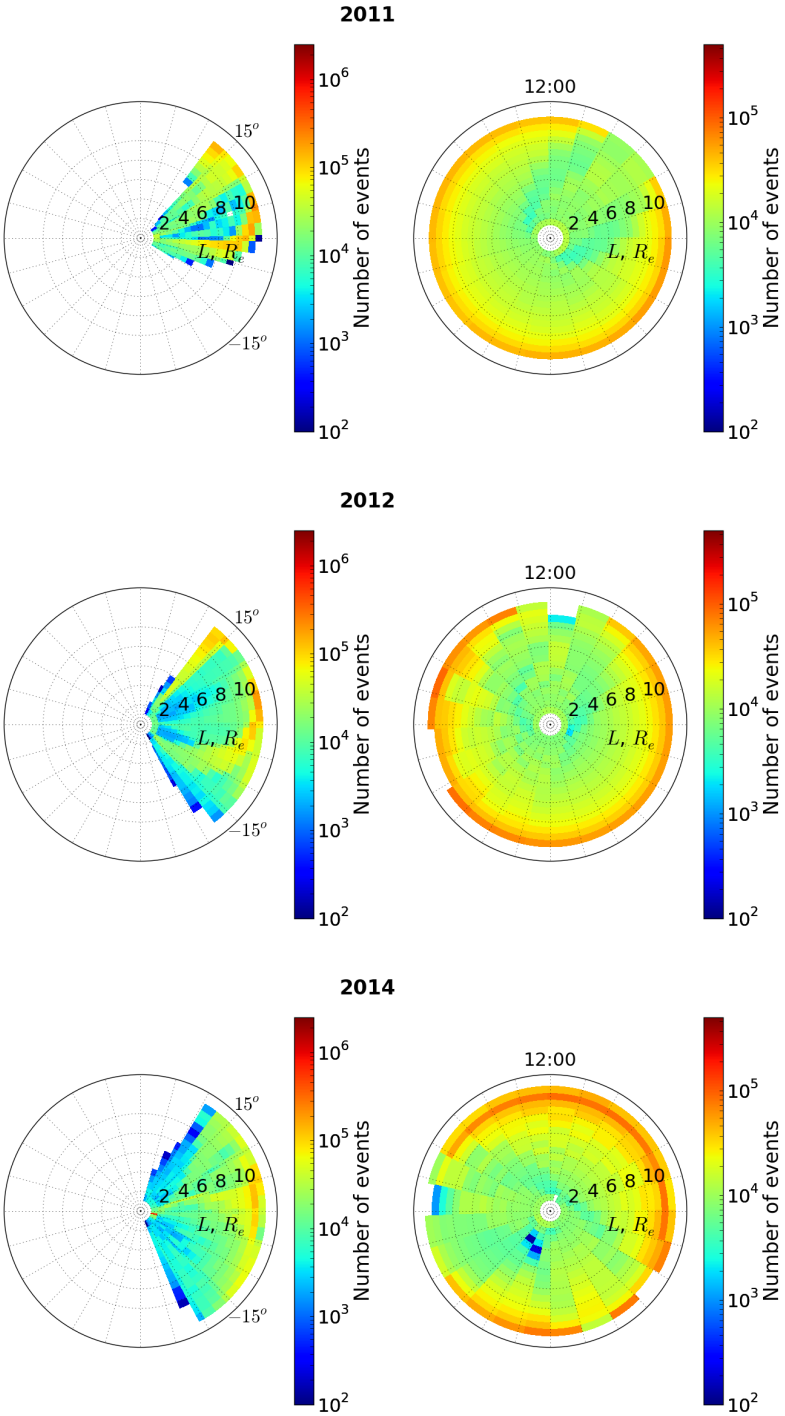

Figure 2: The orbital coverage of THEMIS spacecraft during 2011-2014 within above-specified region by years. The colour coding represents amount of measurements made by the spacecraft in a particular spatial sector.

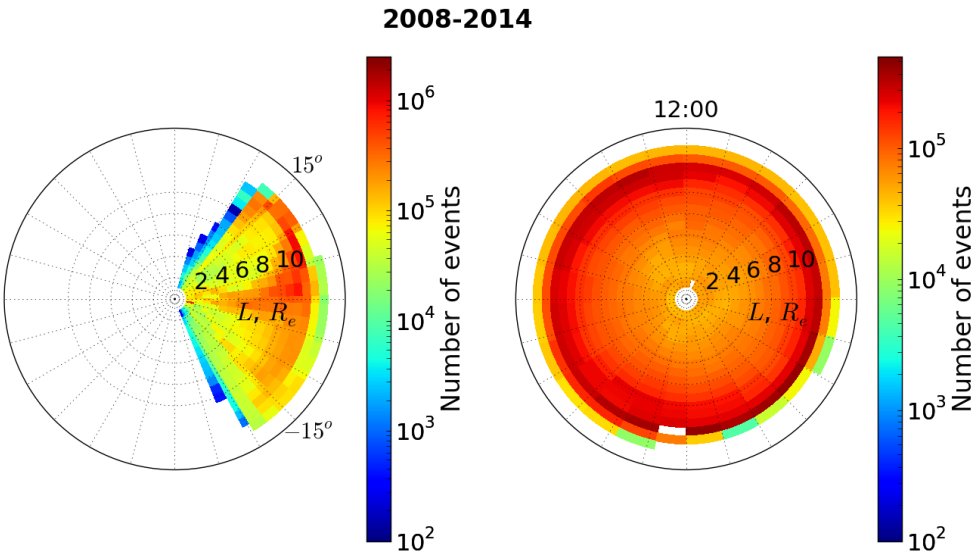

Figure 3: Orbital coverage of THEMIS spacecraft during 2008-2014 within above-specified region. The colour coding represents amount of measurements made by the spacecraft in a particular spatial sector.

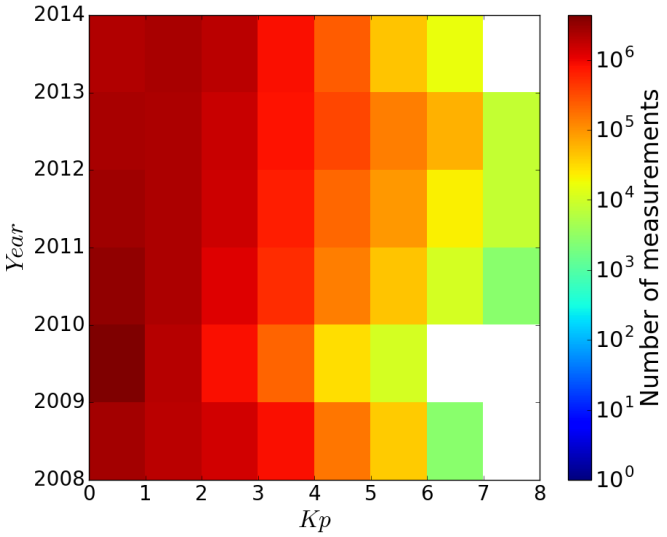

Figure 4: Number of spectra in FBK regime of measurements at different levels of geomagnetic activity registered by THEMIS spacecraft during 2008-2014.

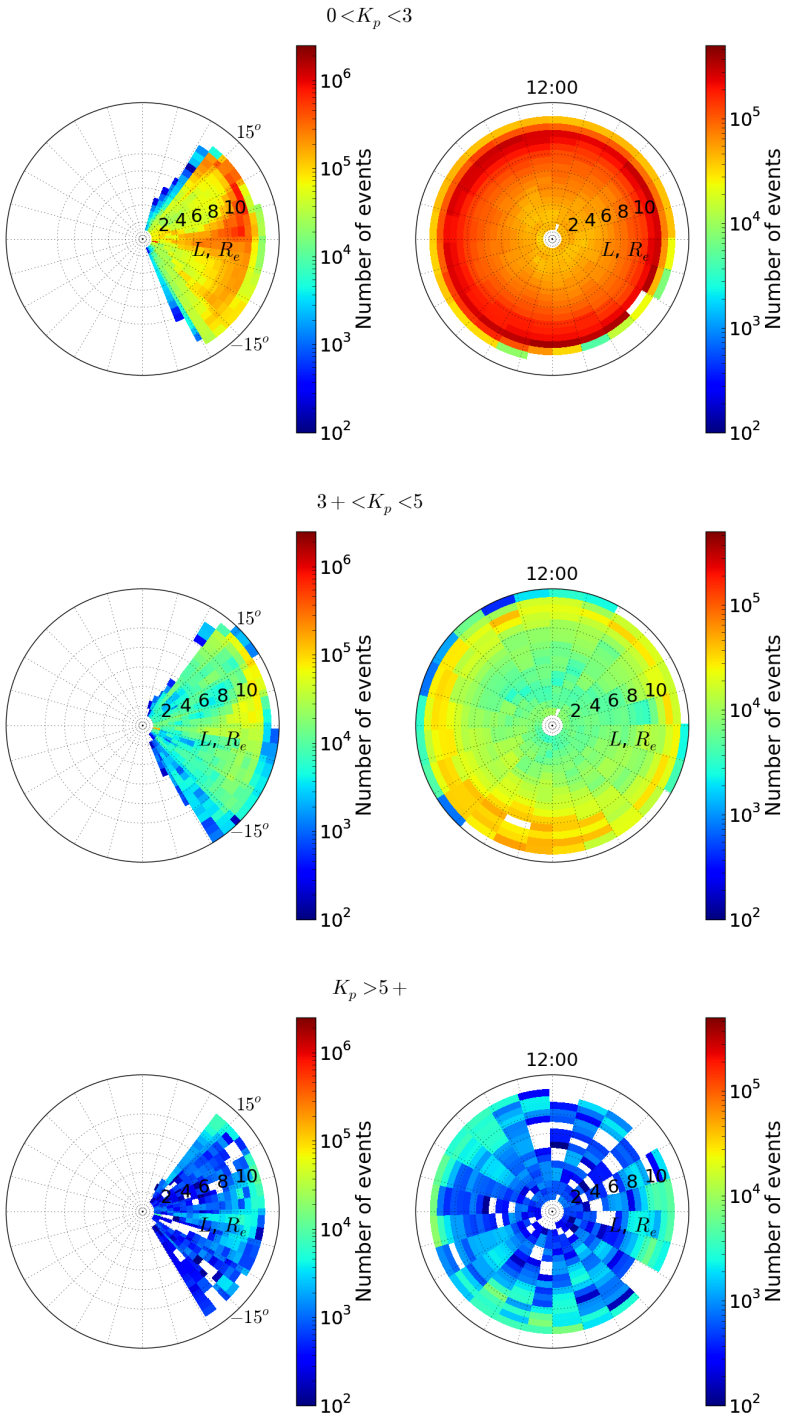

Figure 5: The orbital coverage of THEMIS spacecraft during 2008-2014 within above-specified region corresponding to different levels of geomagnetic activity. The colour coding represents amount of measurements made by the spacecraft in a particular spatial sector.

Band	Frequency range	Sampling rate	No. frequency steps
1	2-4 kHz	1/4 S/s	1
2	0.5-1 kHz	1/4 S/s	1
3	128-256 Hz	1/4 S/s	1
4	32-64 Hz	1/4 S/s	1
5	8-16 Hz	1/4 S/s	1
6	2-4 Hz	1/4 S/s	1

Table 2: Frequency bands of FBK on board of THEMIS spacecraft

consists of three folders ($/tha, /thd, /the$), each folder contains wave events registered by particular spacecraft. Measurements are stored in netcdf v.3.6 files, which have following name convention:

$th\{m\}\_l2s\_fbk\_\{yyyy\}\_\{wave\_type\}.cdf$,

where m - spacecraft mark $\{a, d, e\}$, $yyyy$ - year, when measurements were made $(2008 - 2014)$, $wave\_type$ - type of wave events stored in file. Possible values of wave types are listed in table 7.

Each .cdf file contains several columns which describe spacecraft position, time, geomagnetic activity and amplitude of corresponding emission. Table 3 gives description of available columns in .cdf files.

The dataset was formed on the basis of CDAWeb data. Wave amplitude of particular type were calculated using measurements from six channels of FBK instrument. Signals with amplitude less than 1 pT were interpreted as noise and were extracted from original dataset. Using local value of electron cyclotron frequency f_{ce} 3 frequency bands were determined for magnetosonic ($f < f_{LH}$), hiss ($f_{LH} < f < 0.1 f_{ce}$) and lower band chorus ($0.1 f_{ce} < f < 0.5 f_{ce}$) waves. Wave amplitudes were calculated using signals from channels which central frequency lies within particular frequency band. Resulting wave amplitude

Column	Units	From	To	Description
L		2	8	L-shell value
λ	degrees	-20	20	Magnetic latitude
MLT	hour	0	24	magnetic local time
time	day	1	366	day of the year
BwMSW	nT	10^{-3}	10	Magnetosonic wave amplitude*
BwHISS	nT	10^{-3}	10	Hiss wave amplitude*
BwCHORUS	nT	10^{-3}	10	Lower band chorus amplitude*
KP		0	100	Planetary K_p index
DST				Disturbance storm time index

Table 3: Description of .cdf files. *Each file contains only one of these three fields: BwMSW, BwHISS and BwCHORUS.

was defined as

$$A = \sqrt{\sum_{i=1}^{6} a_i A_i^2},$$

where A_i - signal amplitude of i$-th$ channel and a_i indicates whether signal of i$-th$ channel is used for resulting wave amplitude calculation. For example a_i for lower band chorus are defined as follows:

$$a_i = \begin{cases} 1, f_i \in [0.1 f_{ce}; 0.5 f_{ce}] \\ 0, f_i \notin [0.1 f_{ce}; 0.5 f_{ce}] \end{cases},$$

where f_i - central frequency for i$-th$ channel. Figure 6 shows spatial regions for which a_i is not equal to zero.

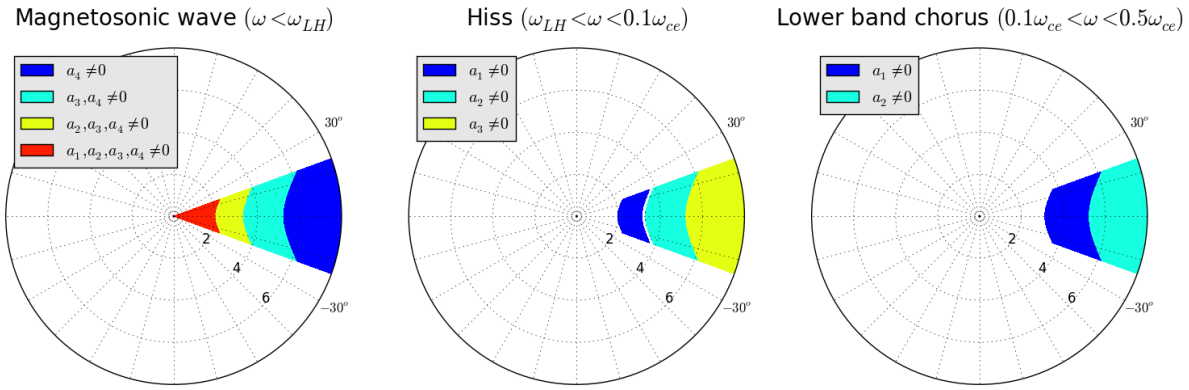

Figure 6: Avaliability of FBK data to process different emissions in L-shell/λ coordinates.

3 Cluster STAFF-SA data description

3.1 Cluster spacecraft

The four-spacecraft Cluster mission launched in pairs in July and August 2000 (Credland *et al.*, 1997; Escoubet *et al.*, 2001). The orbit selected for Cluster is polar, with a perigee of 4 R_E and an apogee of 19,6 R_E. The shape of the four-spacecraft Cluster configuration is basically a tetrahedron which, once set up at a particular point, evolves around the orbit in a deterministic way (Dunlop, 1990). Cluster covered most of the key regions of the magnetosphere: the dayside magnetospheric boundary, both at mid-latitudes and in the cusp, where processes associated with magnetic reconnection and turbulence are believed to occur; the near-Earth magnetospheric tail on the nightside which undergoes frequent largescale magnetic reconfigurations during substorms; and the upstream solar wind, bow shock and magnetosheath. The full covering by Cluster measurements during 2001-2010 is shown in the figure 7 in dependence on the magnetic latitude and magnetic local time.

3.2 Cluster data availability

We made use of the data set of ELF/VLF waves observed by Cluster between February 2001 and December 2010 in the radiation belts (i.e., confined for the $|\lambda| < 45°$ and

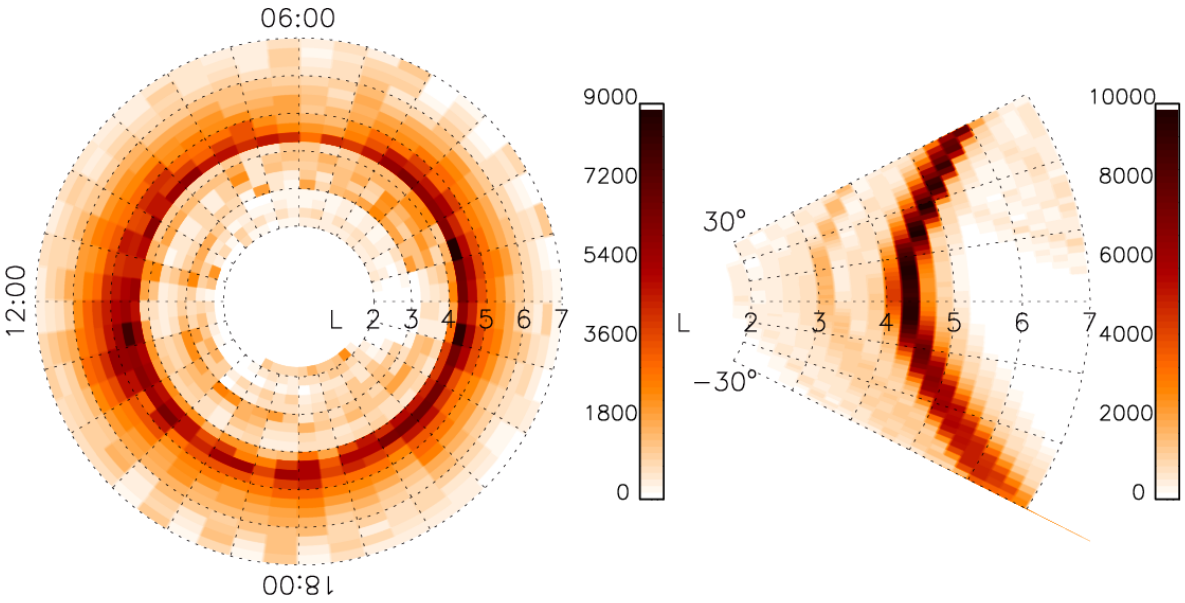

Figure 7: The orbital coverage of Cluster spacecraft during 2001-2010 within above-specified region. The color coding represents relative amount of time the spacecraft spent in a particular spatial sector. The left-hand panel shows the orbital coverage in L-shell/λ coordinates which is obtained by the linear averaging over all MLT values, while the right-hand panel represents the coverage in L-shell/MLT coordinates obtained by averaging over all latitudes along particular L-shell.

$2 < L < 8$). This region is thought to be of primary importance for the generation of chorus waves. The Cluster data set contains a significant number of measurement for the considered range of MLT and L-shells, as illustrated in figure 8.

The analysis is mainly based on data from the spectrum analyzers of the STAFF instruments (Cornilleau-Wehrlin *et al.*, 2003). The STAFF-SA (Spatio-Temporal Analysis of Field Fluctuations - Spectrum Analyzer) experiment (Cornilleau-Wehrlin *et al.*, 1997) includes on-board spectrum analyzer with 27 frequency channels logarithmically spaced between 8.8 Hz and 3.56 kHz. In this deliverable care has been taken to exclude the values of spectral density falling below the magnetometer sensitivity curve presented by (Cornilleau-Wehrlin *et al.*, 2003). The averaged magnetic field intensity is shown in figure 9 and figure 10 for chorus and plasmaspheric hiss, respectively. Tsurutani and Smith (1977) and Meredith *et al.* (2001) showed that chorus can be divided into two categories depending on λ: equatorial $|\lambda| < 15^\circ$ and midlatitude chorus $15^\circ < |\lambda| < 45^\circ$. The distribution properties of these two populations are different. We use here such a separation for L-shell/MLT diagrams for chorus and hiss.

The equatorial LB chorus $|B_w|$ and occurrence rate are shown in figures 9a and 9b for $K_p \leq 3$ and in figures 9c and 9d for $K_p > 3$ in L-shell/MLT frame. Occurrence rate is calculated as the ratio of number of measurements of waves with $|B_w| > 1$ pT on the total number of measurements in each bin. Chorus mainly are observed outside the plasmasphere (modeled plasmapause position is shown by solid line). During quiet conditions, $|B_w|$ are less than 20 pT over the entire region with the maximum in the dawn and pre-noon sector at $6 < L < 8$. Intense waves are observed also on $L > 9$, from 10:00 to 14:00 MLT, possibly connected to secondary chorus sources in the dayside magnetic field pockets (Tsurutani and Smith, 1977). Occurrence rate is quite close to the observed by THEMIS spacecraft in the equatorial region (Cully *et al.*, 2008; Li *et al.*, 2011; Meredith *et al.*, 2012). The midlatitude LB chorus intensity and occurrence rate are shown in figures 9e and 9f. The spatial dependence of the distribution is different

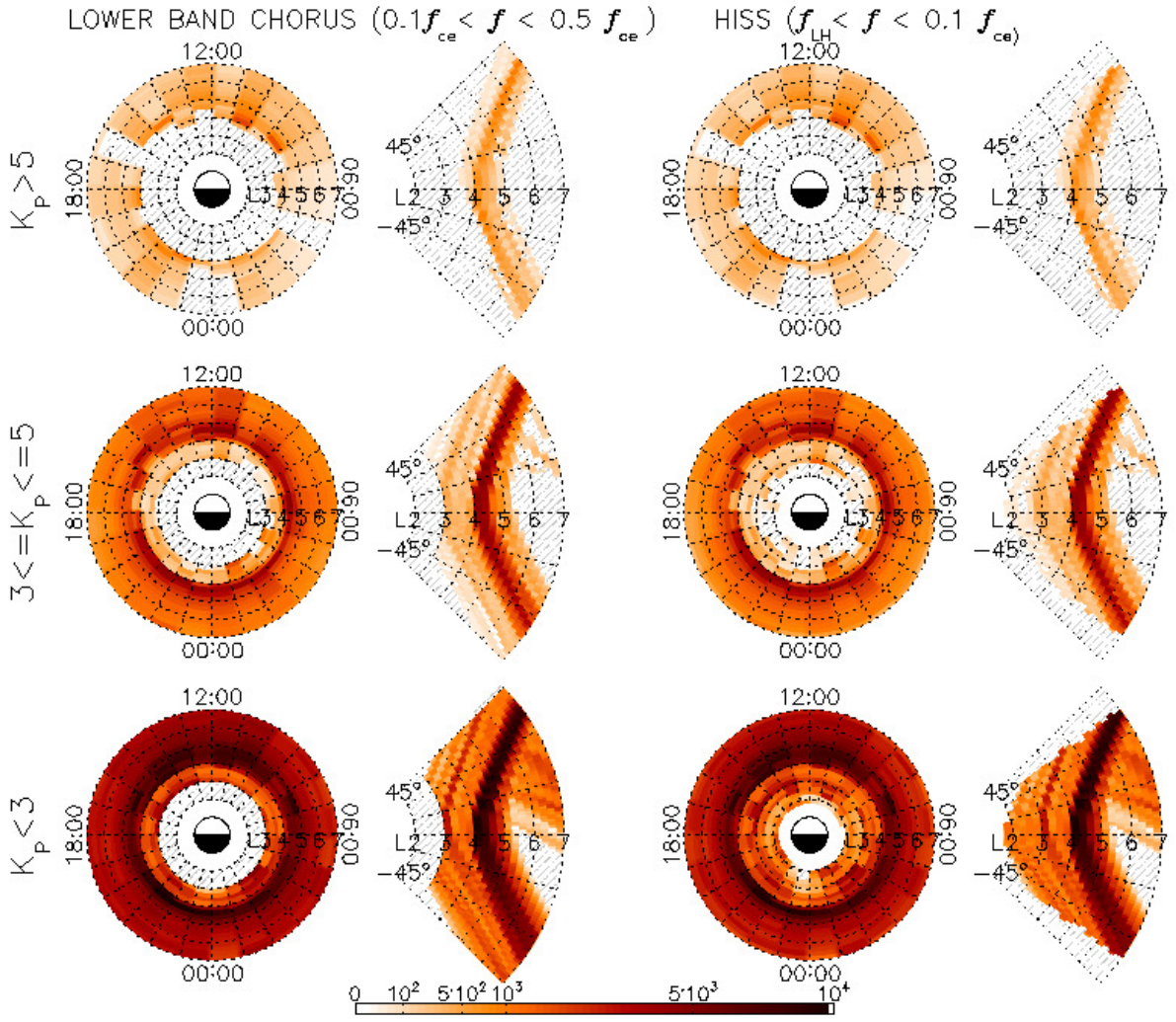

Figure 8: Data coverage for the Cluster STAFF-SA measurements during 2001-2010 (left panels) for the LB chorus frequency range ($0.1f_{ce} < f < 0.5f_{ce}$) and (right panels) for the hiss frequency range ($f_{LH} < f < 0.1f_{ce}$) in dependence on L-shell, (bottom panels) λ and MLT for periods of low ($K_p < 3$), (top panels) intermediate ($3 \leq K_p \leq 5$) and high geomagnetic activity ($K_p > 5$) (figure taken from (Agapitov *et al.*, 2013)).

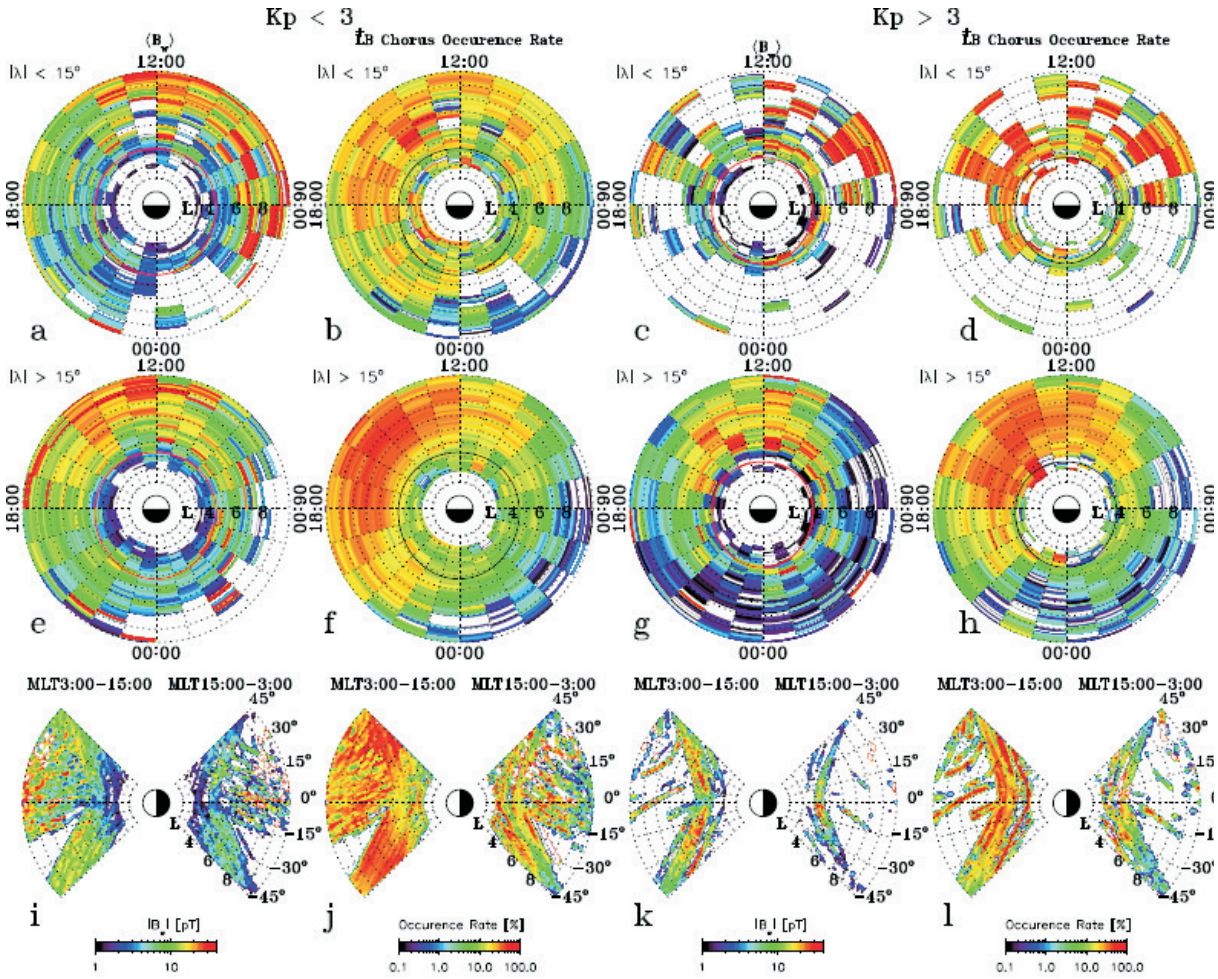

Figure 9: (a) Cluster measurements of equatorial chorus averaged wave intensity and (b) occurrence rate shown in L-shell/MLT frame for quiet geomagnetic conditions ($K_p \leq 3$). (c and d) Distributions of averaged intensity and occurrence rate for disturbed conditions ($K_p > 3$) are shown, respectively. Distributions for midlatitude chorus are shown in figures 9e and 9f $K_p \leq 3$ and 9g and 9h $K_p > 3$ in the same format. (i) Chorus averaged wave intensity and (j) occurrence rate are shown in L-shell/λ frame for $K_p \leq 3$, figures 9k and 9l, respectively, show distributions for $K_p > 3$ (figure taken from (Agapitov *et al.*, 2013)).

from the equatorial LB chorus. The amplitudes are close, but the peak of intensity is shifted to the afternoon sector 12:00-15:00 MLT and $6 < L < 10$ with larger occurrence rate ($> 60\%$).

The LB chorus statistics for $K_p > 3$ is poor (especially in the vicinity of the equator): It can be seen that amplitudes and occurrence rate of equatorial LB chorus are generally larger than during low geomagnetic activity (up to 50 pT). Waves with amplitudes greater than 1 pT are observed closer to the Earth near the position of the plasmapause. At $4 < L < 5$, Cluster STAFF-SA measurement coverage is good, and for this range of L-shell, the distribution of $|Bw|$ dependence on MLT has maximal values from 02:00 to 14:00 MLT. The most intense chorus are observed in the outer magnetosphere ($L > 6$) in the pre-noon sector (here it can be caused by measurement gap especially for $L > 5$). The Cluster STAFF-SA measurement coverage for $|\lambda| > 15^\circ$ is sufficient for statistical analysis. Midlatitude LB chorus during high geomagnetic activity has maximum in intensity at $L \sim 5 - 6$, 10:00-14:00 MLT. The intensity and occurrence rate peaks are closer to the Earth than they are during quiet geomagnetic activity.

The dependence of chorus magnetic field averaged intensity and chorus occurrence rate in L-shell/λ frame is presented in figures 9i- 9l. The magnetic field amplitude minimum is obtained in the day and night sectors at L-shells from 4 to 6 during the quiet geomagnetic conditions ($K_p \leq 3$). Magnetic field amplitude maximum is observed at $\lambda \sim 10^\circ - 20^\circ$ and above $25^\circ - 30^\circ$ $|B_w|$ decreases. This $|Bw|$ maximum shifts toward the Earth during high geomagnetic activity and is observed at $L \sim 4 - 5$ and $|\lambda| < 15^\circ$. LB chorus occurrence rate is high for all λ in the day sector for $5 < L < 10$ during low geomagnetic activity and for $4 < L < 8$ for $K_p > 3$. In the night sector, occurrence rate generally is lower and has maximal values $\sim 60\%$ at $4 < L < 8$ for $K_p \leq 3$ and $4 < L < 6$ for $K_p > 3$.

The plasmaspheric hiss $|Bw|$ and occurrence rate are shown in figures 10a and 10b for $K_p \leq 3$ and in figures 10c and 10d for $K_p > 3$ in L-shell/MLT frame. High amplitude hiss waves are principally observed at 10:00-22:00 MLT with intensity maximum about

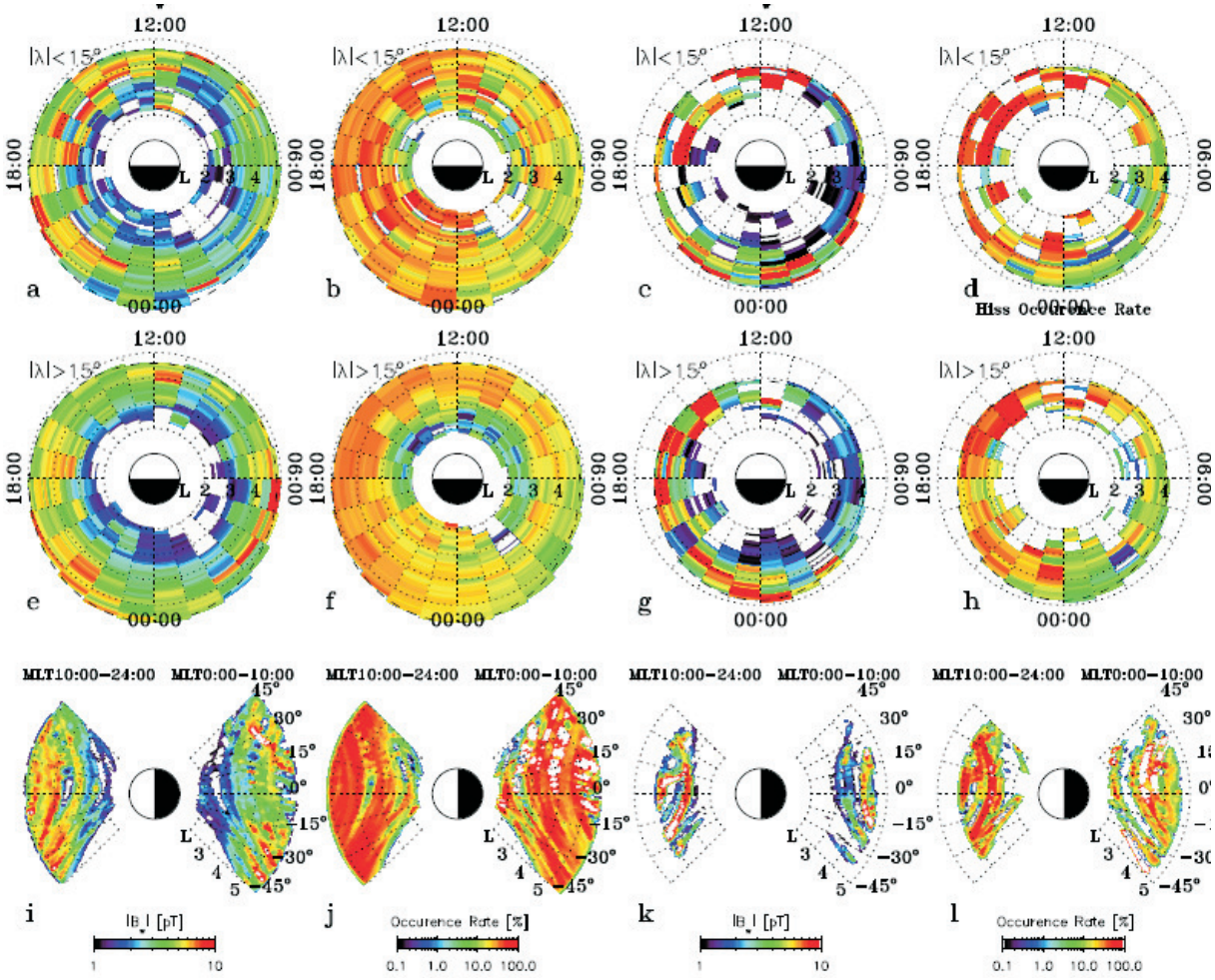

Figure 10: The averaged Cluster wave magnetic field intensity and occurrence rate of plasmaspheric hiss in the same format as in figure 9 (figure taken from (Agapitov *et al.*, 2013)).

year-mm-dd	hh:mm:ss	L-shell	λ	MLT	B_w	Dst	K_p
2010-04-29	04:53:18	4.8809	0.2663	12.1497	6.9951	7	33

Table 4: .dat files format description.

10 pT at $4 < L < 5$ during quiet geomagnetic activity and up to 15 pT at $3 < L < 4$ during high. Maximum of the occurrence rate MLT is shifted during high geomagnetic activity periods from 13:00-24:00 to 10:00-20:00 MLT. The equatorial and midlatitude distributions do not differ significantly (as well as the occurrence rate), but amplitudes of midlatitude plasmaspheric hiss are generally smaller than equatorial values. The intense waves observed from 02:00 to 06:00 MLT (figure 10e) can be LB chorus waves propagating near the plasmapause.

The plasmaspheric hiss intensity and occurrence rate distribution in L-shell/λ frame distribution show rather constant wave amplitude values for different λ (figures 10i- 10l) and intensity peak at $3 < L < 5$ with high occurrence rate during low and high geomagnetic activity ($> 50\%$).

3.3 Cluster database description

The database contains measurements of lower band chorus, hiss and magnetosomic events of 4 Cluster spacecraft during 2001-2010. Database consists of three files, each file contains wave events of particular type registered onboard of spacecraft. MSW.dat, HISS.dat and LBChorus.dat files contain magnetosonic, hiss and lower band chorus events respectively. Measurements are stored in .dat files in ASCII format described by table 4.

Each .dat file contains several columns which describe spacecraft position, time, geomagnetic activity and amplitude of corresponding emission. Table 5 gives description of available columns in .dat files.

The dataset was formed on the basis of CDAWeb data. Wave amplitude of particular type were calculated using measurements from 27 channels of STAFF-SA instrument. Signals with amplitude less than 1 pT were interpreted as noise and were extracted from

Column	Units	From	To	Description
year-mm-dd		2001-02-01	2010-04-30	Date
hh:mm:ss		00:00:00	23:59:59	Time
L-shell		3	5	L-shell value
λ	degrees	-20	20	Magnetic latitude
MLT	hour	10	16	magnetic local time
Bw	pT	1	10^4	Wave amplitude
KP		0	100	Planetary K_p index
DST				Disturbance storm time index

Table 5: Description of .dat file.

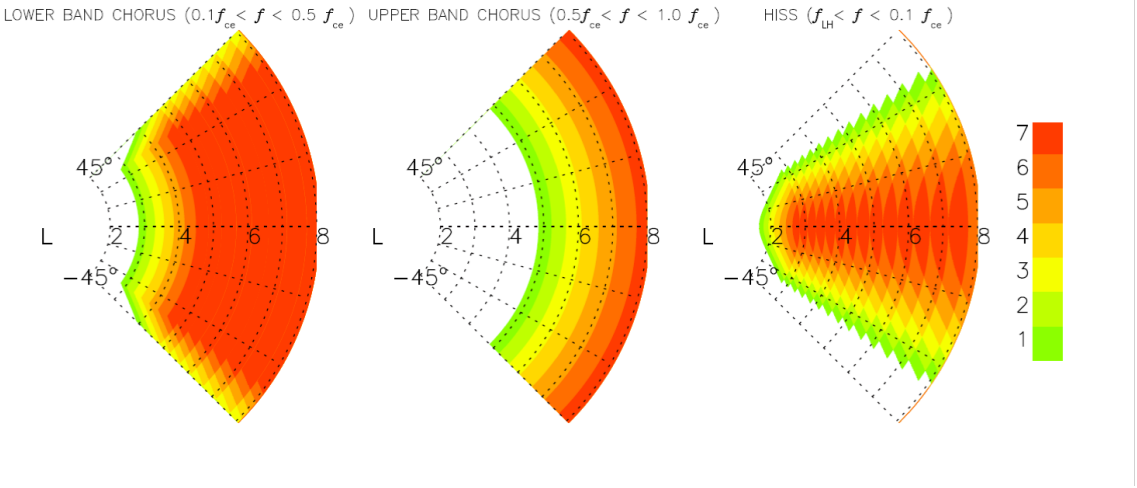

Figure 11: Avaliability of STAFF-SA data to process different emissions.

original dataset. Using local value of electron cyclotron frequency f_{ce} 3 frequency bands were determined for magnetosonic ($f < f_{LH}$), hiss ($f_{LH} < f < 0.1 f_{ce}$) and lower band chorus ($0.1 f_{ce} < f < 0.5 f_{ce}$) waves. Wave amplitudes were calculated using similar procedure described in section 2.3. Figure 11 shows number of channels available for detecting wave emissions of particular type.

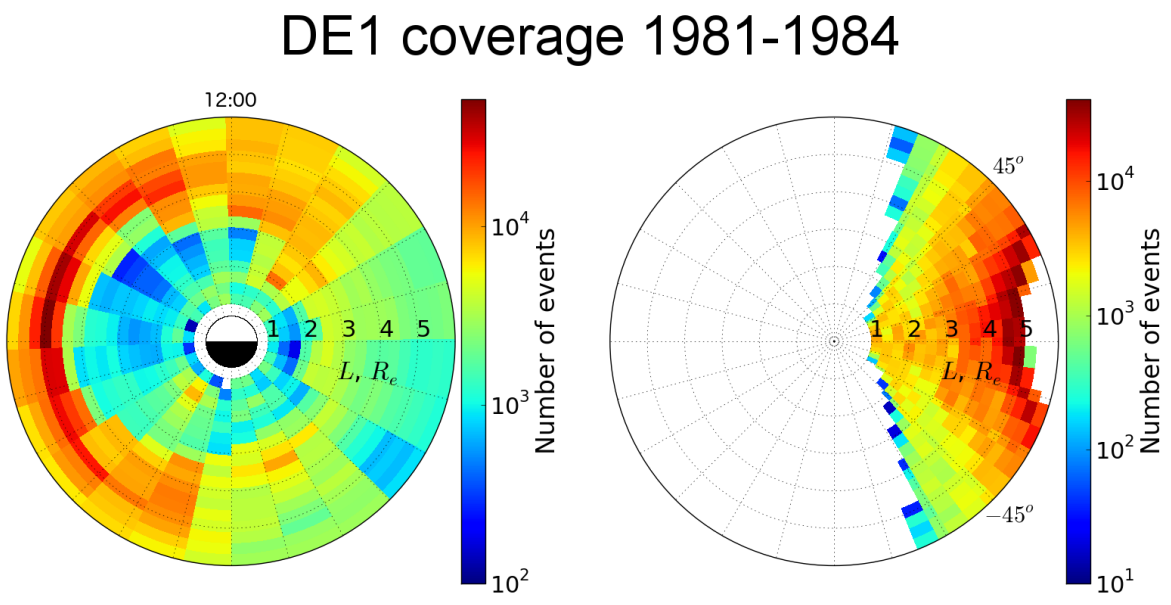

Figure 12: Coverage of the DE-1 PWI measurements during 1981-1984.

4 DE-1 PWI data description

4.1 DE-1 spacecraft

The Dynamics Explorer 1 (DE-1) mission's general objective is to investigate the strong interactive processes coupling the hot, tenuous, convecting plasmas of the magnetosphere and the cooler, denser plasmas and gases corotating in the earth's ionosphere, upper atmosphere, and plasmasphere (Gurnett and Inan, 1988).

The DE-1 spacecraft (high-altitude mission) was launched on August 3, 1981 into an initial orbit with perigee of 568 km and apogee 23,289 km (3.65 R_E), inclination 90°. The argument of perigee advances at a rate of 108° per year thus enabling a complete coverage in longitude within 3 years. On October 22, 1990 science operations were terminated.

The Plasma Wave Instrument (PWI) measured AC electric fields over the frequency range from 1 Hz to 2 MHz, and an amplitude range of 0.03 microvolt per meter to 100 mV per meter. Magnetic fields were measured from 1 Hz to 400 kHz over an approximately 100-dB range. The sweep frequency receiver's (SFR) data consists of measurements from

Band	Frequency range	Bandwidth	Dwell time	No. frequency steps
1	1-792 Hz	8 Hz	32 s	32
2	1.18-6.67 kHz	54 Hz	32 s	32
3	7.23-51.2 kHz	440 Hz	32 s	32
4	58-410 kHz	3.5 kHz	32 s	32

Table 6: Frequency bands of PWI SFR on board of DE-1 spacecraft

a 128 logarithmically spaced frequency bands with 1% resolution ranging in frequency from 104 Hz to 410 kHz. Table 6 summarises primary characteristics of the PWI SFR instrument.

4.2 DE-1 data availability

We made use of the data set of ELF/VLF waves observed by DE-1 between September 1981 and June 1984 in the radiation belts (i.e., confined for the $|\lambda| < 20^\circ$ and $2 < L < 8$). The coverage by DE-1 measurements during 1981-1984 is shown in figure 12.The analysis is based on data from the SFR of the PWI instrument. Distributions of spectral density of magnetic field of LB chorus $|B_w|$ are shown in figures 13a for $K_p \leq 3$, 13b for $3 \leq K_p < 5$ and 13c for $K_p \geq 5$ in L-shell/MLT frame. Distributions in L-shell/λ and L-shell/MLT frames have been computed, respectively, by the averaging over all MLT and λ values. During quiet conditions, the maximum of LB chorus is located in the dawn and pre-dusk sector at $5 < L < 6$. It can be seen that amplitudes of LB chorus are generally larger during high geomagnetic activity, the high-amplitude LB chorus are registered in the broad region $4 < L < 6$ covering dawn and post-noon sectors. High-amplitudes waves are observed closer to the Earth near the position of the plasmapause. At $4 < L < 5$, DE-1 PWI measurement coverage is good, and for this range of L-shell, the distribution of $|Bw|$ dependence on MLT has maximal values from 06:00 to 15:00 MLT.

The dependence of chorus magnetic field spectral density in L-shell/λ frame is presented in figures 13d- 13f. The minimum of magnetic field spectral density is obtained at

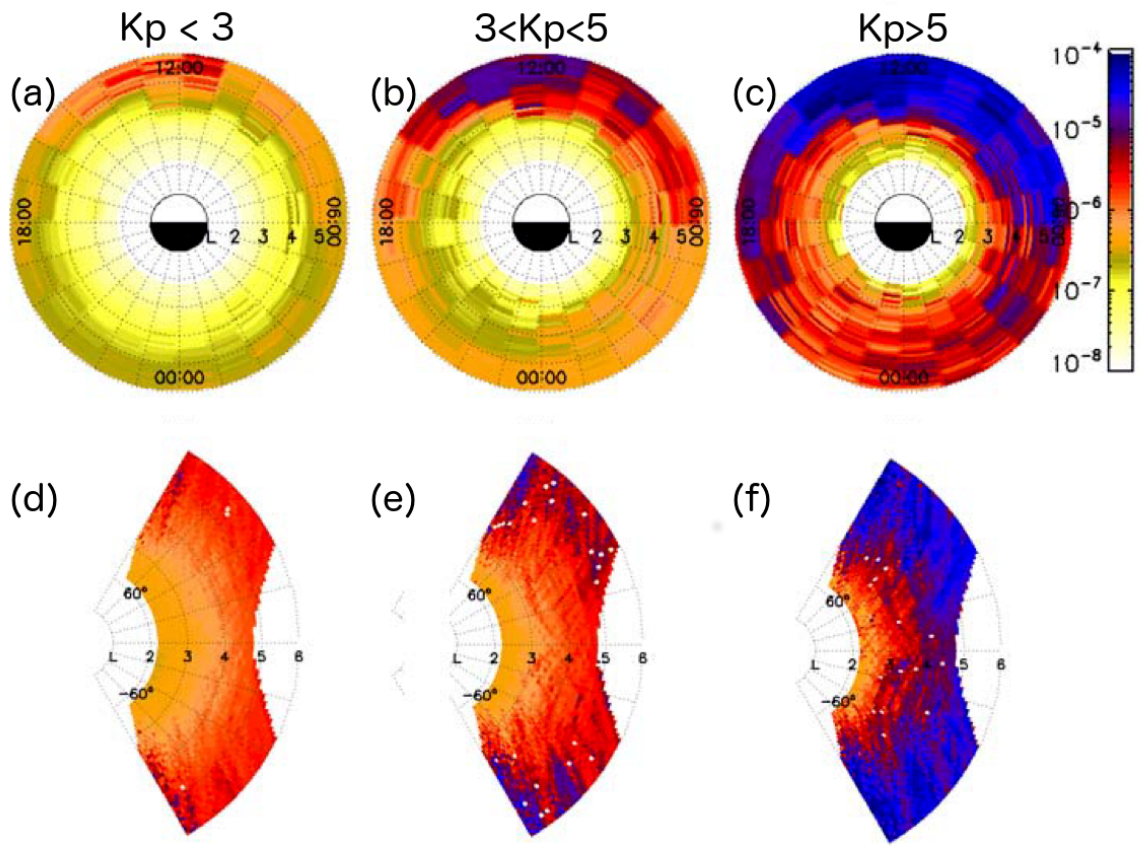

Figure 13: (a) Equatorial chorus averaged wave intensity in L-shell/MLT and (d) in L-shell/λ frames for quiet geomagnetic conditions ($K_p \leq 3$). (b and e) Distributions of averaged intensity in L-shell/MLT and in L-shell/λ frames for intermediate ($3 < K_p \leq 5$) and (c and f) high geomagnetic activity ($K_p > 5$), respectively. Figures are obtained using measurements registered by PWI instrument on board DE-1 spacecraft during 1981-1984.

L-shells from 2 to 5 near equator during the quiet and disturbed geomagnetic conditions. The maximum is observed at at L-shells from 4 to 5 covering $\lambda \sim 15° - 60°$. This $|Bw|$ maximum shifts toward the Earth during high geomagnetic activity and is observed at $L \sim 4 - 5$ and $|\lambda| < 15°$.

The spectral density of magnetic field is shown in figure 14 for hiss emissions. The spectral density of magnetic field intensities of hiss $|B_w|$ are shown in figures 14a for $K_p \leq 3$, 14b for $3 \leq K_p < 5$ and 14c for $K_p \geq 5$ in L-shell/MLT frame. During quiet conditions, the maximum of hiss emissions is located in the noon and pre-dusk sector at $4 < L < 5$. It can be seen that amplitudes of hiss are generally larger during high geomagnetic activity, the high-amplitude hiss emissions are registered in the broad region

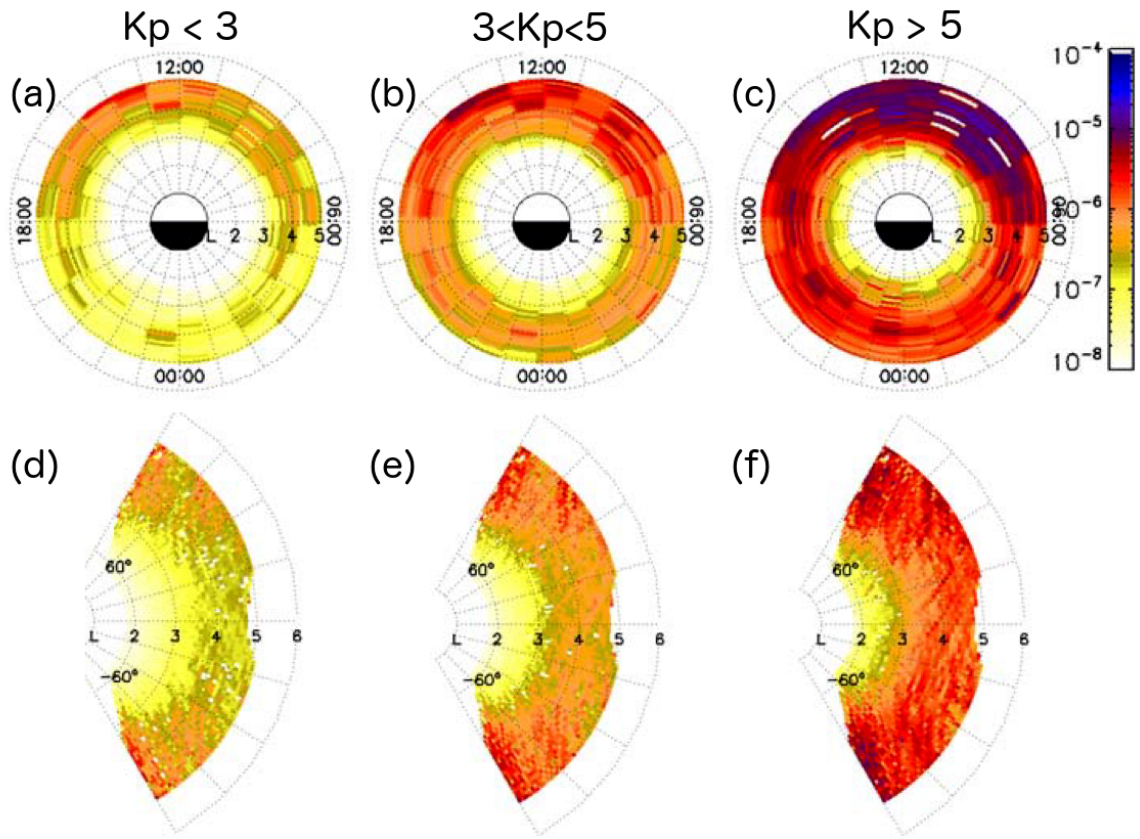

Figure 14: Distribution of the spectral density of magnetic field for plasmaspheric hiss emissions in L-shell/λ and L-shell/MLT frames in the same format as in figure 13. Figures are obtained using measurements registered by PWI instrument on board DE-1 spacecraft during 1981-1984.

$3 < L < 6$ covering dawn and post-noon sectors. High-amplitudes waves are observed in the plasmasphere. At $3 < L < 5$, the distribution of $|Bw|$ dependence on MLT has maximal values from 07:00 to 13:00 MLT.

The dependence of chorus magnetic field spectral density in L-shell/λ frame is presented in figures 14d- 14f. The magnetic field minimum is obtained at L-shells from 2 to 4 near equator during the quiet geomagnetic conditions. The maximum of the spectral density is observed at L-shells from 4 to 5 covering $\lambda \sim 30° - 60°$. This $|Bw|$ maximum shifts toward lower λ and is observed at the equator during high geomagnetic activity and at $L \sim 3 - 5$.

The spectral density of magnetic field is shown in figure 15 for magnetosonic waves.

The spectral density of magnetic field of magnetosonic waves $|B_w|$ are shown in figures 15a for $K_p \leq 3$, 15b for $3 \leq K_p < 5$ and 15c for $K_p \geq 5$ in L-shell/MLT frame. During quiet conditions, the maximum of magnetosonic waves is located in the noon and pre-dusk sector at $2 < L < 4$. It can be seen that amplitudes of magnetosonic waves are generally larger during high geomagnetic activity, the high-amplitude magnetosonic waves are registered at $2 < L < 4$ covering dawn and post-noon sectors. The distribution of $|Bw|$ dependence on MLT has maximal values from 06:00 to 15:00 MLT.

The dependence of spectral density of magnetosonic waves in L-shell/λ frame is presented in figures 15d- 15f. The magnetic field amplitude is uniform showing several peaks at $\lambda \sim 15^\circ - 30^\circ$ during the quiet geomagnetic conditions. During high geomagnetic activity magnetic field amplitude maximum is observed at at L-shells from 4 to 5 covering $\lambda \sim 30^\circ - 45^\circ$.

4.3 DE-1 database description

The database contains measurements of SFR and LFC instruments of DE-1 spacecraft from September 1981 to June 1984. Database consists of twelve files, each file contains wave events registered during one year. Measurements are stored in netcdf v.3.6 files, which have following name convention:

$de\_\{wave\_type\}\_\{yyyy\}.cdf$,

where $yyyy$ - year, when measurements were made $(1981 - 1984)$, $wave\_type$ - type of wave events stored in file. Using local value of electron cyclotron frequency f_{ce} 3 frequency bands were determined for magnetosonic ($f < f_{LH}$), hiss ($f_{LH} < f < 0.1 f_{ce}$) and lower band chorus ($0.1 f_{ce} < f < 0.5 f_{ce}$) waves.

Each .cdf file contains several columns which describe spacecraft position, time, geomagnetic activity and amplitude of corresponding emission. Table 8 gives description of available columns in .cdf files.

The dataset was formed on the basis of CDAWeb data. Signals with intensity less than 10^{-9} nT^2/Hz were interpreted as noise and were extracted from original dataset.

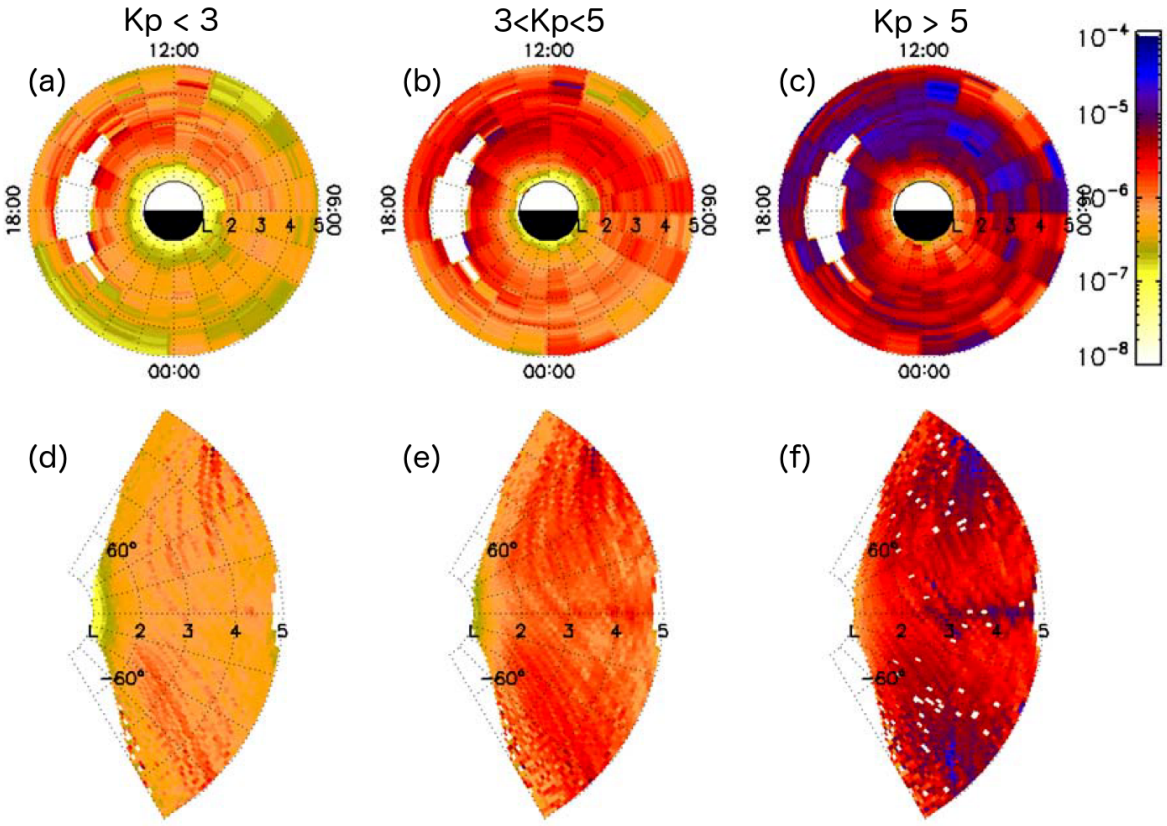

Figure 15: Distribution of the spectral density of magnetic field for magnetosonic wave in and L-shell/MLT frame in the same format as in figure 13. Figures are obtained using measurements registered by PWI instrument on board DE-1 spacecraft during 1981-1984.

Abbreviation	Description
msw	Magnetosonic waves
hiss	Hiss waves
lbc	Lower band chorus

Table 7: Description of wave types

Column	Units	From	To	Description
L		2	8	L-shell value
λ	degrees	-20	20	Magnetic latitude
MLT	hour	0	24	magnetic local time
time	day	1	366	day of the year
B	nT^2/Hz	10^{-9}	1	Emission intensity
FR	Hz	1.78	$4.1 \cdot 10^5$	Frequency
KP		0	100	Planetary K_p index
DST				Disturbance storm time index

Table 8: Description of DE-1 .cdf file.

All intervals with anomalously high magnitudes of spectral density were eliminated. On average about 30% of the data has been thrown away during this quality check process.

5 Polar PWI data description

5.1 Polar Spacecraft

The launch of the Polar spacecraft took place on February 24, 1996. The initial orbit of Polar had a perigee at 185 km altitude and an apogee of 55, 550 km and the inclination of 86°. The Polar wave data were collected by the PWI instrument which operated between February 27, 1996 and September 16, 1997 when the instrument failed. All 5 PWI receivers (Sweep Frequency Receiver (SFR), Multi-Channel Analyzer, Wideband Receiver, High Frequency Waveform Receiver, and Low Frequency Waveform Receiver) were functioning nominally until the instrument failed. SFR data will be used in the WP4. Table 9 contains information of main parameters of SFR used to create the database.

5.2 Polar data availability

The coverage by Polar spacecraft during the period of PWI operation October 1996 - February 1997 is shown in figure 16.

Band	Frequency range	Bandwidth	Dwell time	Response time	No. frequency steps
1	24-200 Hz	5 Hz	1.03 s	1 s	32
2	200-1600 Hz	15.6 Hz	515.2 ms	382 ms	32
3	1.6-12.5 kHz	125 Hz	257.6 ms	177 ms	32
4	12.5-100 kHz	1 kHz	36.8 ms	24 ms	64
5	100-800 kHz	8 kHz	36.8 ms	14 ms	64

Table 9: Frequency bands of PWI SFR on board of Polar spacecraft

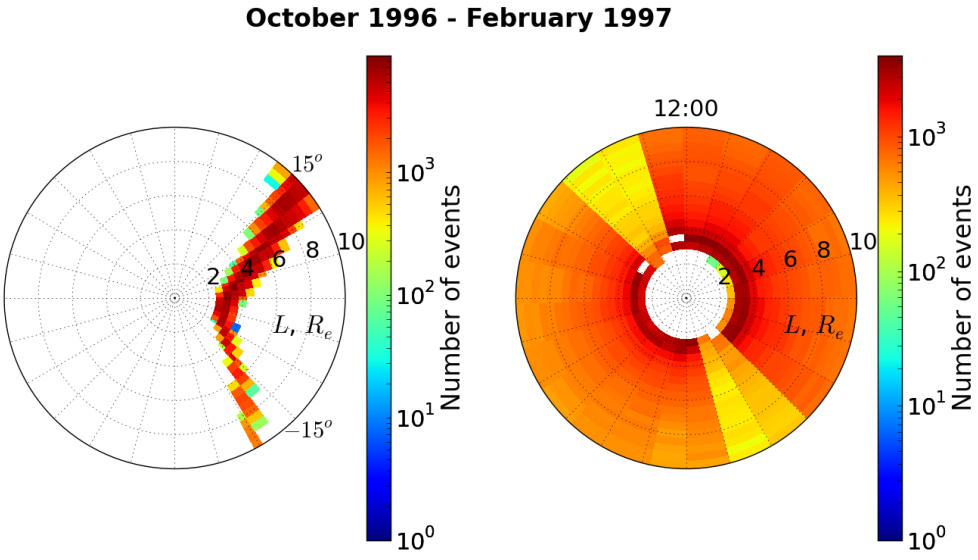

Figure 16: Orbital coverage of Polar spacecraft during 1996-1997. The colour coding represents amount of measurements made by the spacecraft in a particular spatial sector.

The coverage of Polar during this period of PWI operation, grouped according to K_p (low $0 \leq K_p < 3$, medium $3 \leq K_p < 5$ and high activity levels $K_p \geq 5$) are shown on figure 17. The colour coding represents number of measurements spacecraft made in a particular spatial sector during 1996-1997. The left-hand panel shows the orbital coverage in L-shell/λ coordinates which is obtained by summation over all MLT values, while the right-hand panel represents the coverage in L-shell/MLT coordinates obtained by summation over all latitudes along particular L-shell. As geomagnetic activity increases, the data coverage reduces considerably due to the rarity of such periods. Due to short operation time of Polar spacecraft the data coverage in L-shell/MLT frame is not complete. The amount of data from Polar is small when compared with that available from Cluster and THEMIS.

5.3 Polar database description

The database contains measurements of SFR instrument of Polar spacecraft from October 1996 to February 1997. Measurements are stored in three files, each file contains wave events of particular type registered onboard of spacecraft. *polar_msw_pwi.dat*, *polar_hiss_pwi.dat* and *polar_lbc_pwi.dat* files contain magnetosonic, hiss and lower band chorus events respectively. The file contains several columns which describe spacecraft position, time, geomagnetic activity and amplitude of corresponding emission. Table 10 gives description of available columns in .cdf file.

The dataset was formed on the basis of CDAWeb data. Signals with intensity less than 10^{-9} nT^2/Hz were interpreted as noise and were extracted from original dataset. We separate the entire dataset into 96 frequency channels logarithmically spaced in the frequency range from 24 Hz to 12.5 kHz. Each frequency channel was then scanned in order to eliminate all intervals with anomalously high magnitudes of spectral density. On average about 20% of the data has been thrown away during this quality check process.

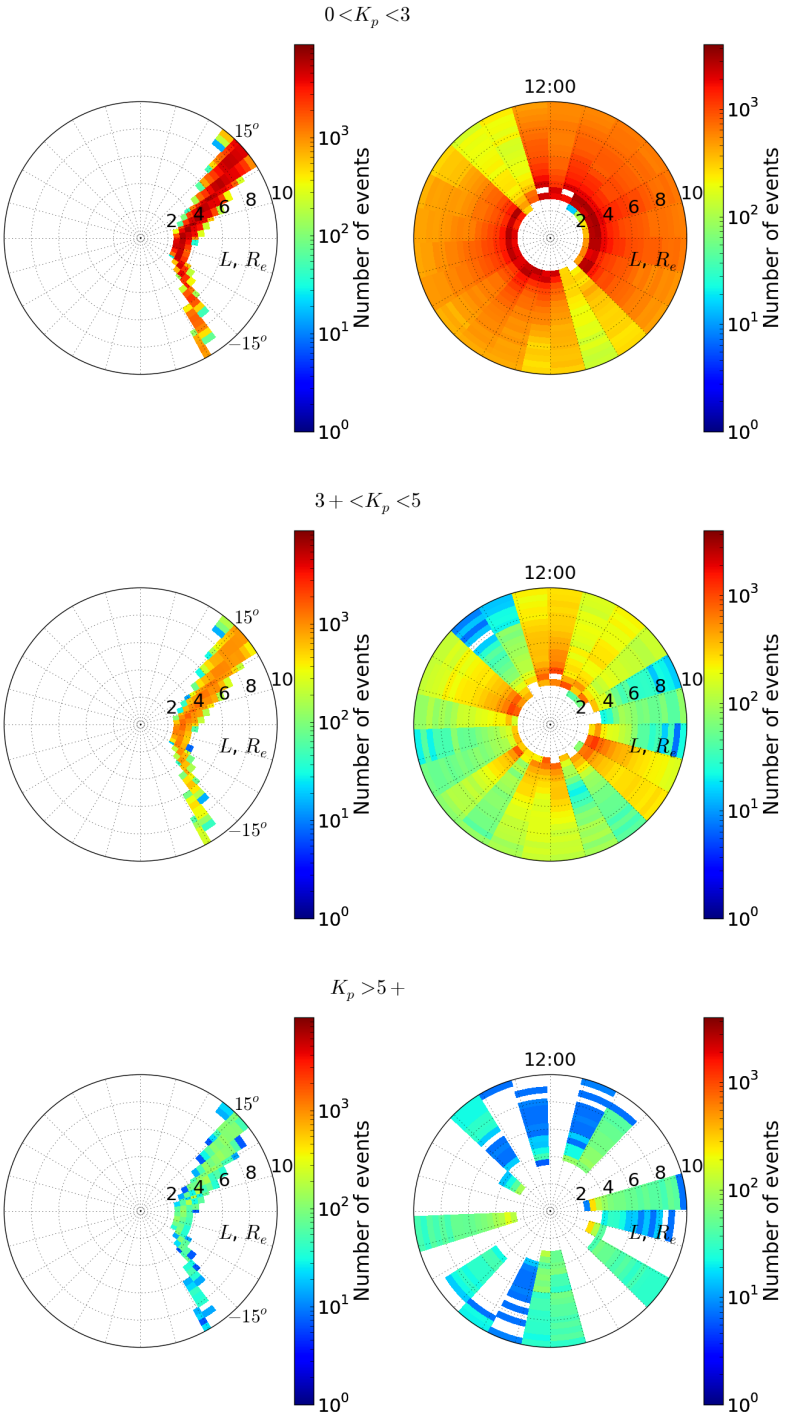

Figure 17: The orbital coverage of Polar spacecraft during 1996-1997 corresponding to different levels of geomagnetic activity. The colour coding represents amount of measurements made by the spacecraft in a particular spatial sector.

Column	Units	From	To	Description
L		2	8	L-shell value
λ	degrees	-20	20	Magnetic latitude
MLT	hour	0	24	magnetic local time
Epoch	date	01/10/1996	28/02/1997	Date and time for SFR Band 1
Epoch2	date	01/10/1996	28/02/1997	Date and time for SFR Band 2
Epoch3	date	01/10/1996	28/02/1997	Date and time for SFR Band 3
SFR1B	nT^2/Hz	10^{-9}	1	Emission intensity for SFR Band 1
SFR2B	nT^2/Hz	10^{-9}	1	Emission intensity for SFR Band 2
SFR3B	nT^2/Hz	10^{-9}	1	Emission intensity for SFR Band 3
Frequency1	Hz	24	200	Frequency for 32 channels of SFR Band 1
Frequency2	Hz	200	1600	Frequency for 32 channels of SFR Band 2
Frequency3	Hz	1600	$12.5 \cdot 10^3$	Frequency for 32 channels of SFR Band 3
KP		0	100	Planetary K_p index
DST				Disturbance storm time index

Table 10: Description of Polar .cdf file.

6 CRRES PWE data description

6.1 CRRES spacecraft

CRRES spacecraft, launched on July 25, 1990, had a perigee at 350 km altitude and an apogee of 6.3 Re, and the inclination of 18.2°. The CRRES orbit was similar to the geosynchronous transfer orbit. The aims of the CRRES mission included studies of the natural radiation belts, effects of high energy on spacecraft hardware performance.

The CRRES plasma wave experiment (PWE) instrumentation has been designed to measure the plasma wave environment in the Earth's radiation belts with emphasis on high-frequency and time resolution, a large dynamic range, and sufficient frequency response to cover all of the characteristic frequencies of the plasma that are of interest (Anderson *et al.*, 1992). The CRRES plasma wave experiment provides measurements of electric fields from 5.6 Hz to 400 kHz.

The data from the CRRES plasma wave experiment used in this study come from the sweep frequency receiver (SFR) that provided high-frequency resolution spectrum measurements from 100 Hz to 400 kHz. The dynamic range for each of the receivers is about 100 dB beginning at the respective receiver's noise level. The sweep frequency receiver covers the frequency range from 100 Hz to 400 kHz in four bands with 32 steps per band. Table 11 describes main characteristics of SFR receiver.

Band	Frequency range	Response time	No. frequency steps
1	100-800 Hz	1 channels/s	32
2	800-6.4 kHz	2 channels/s	32
3	6.4-50 kHz	4 channels/s	32
4	50-400 kHz	4 channels/s	32

Table 11: Frequency bands of PWE SFR on board of CRRES spacecraft

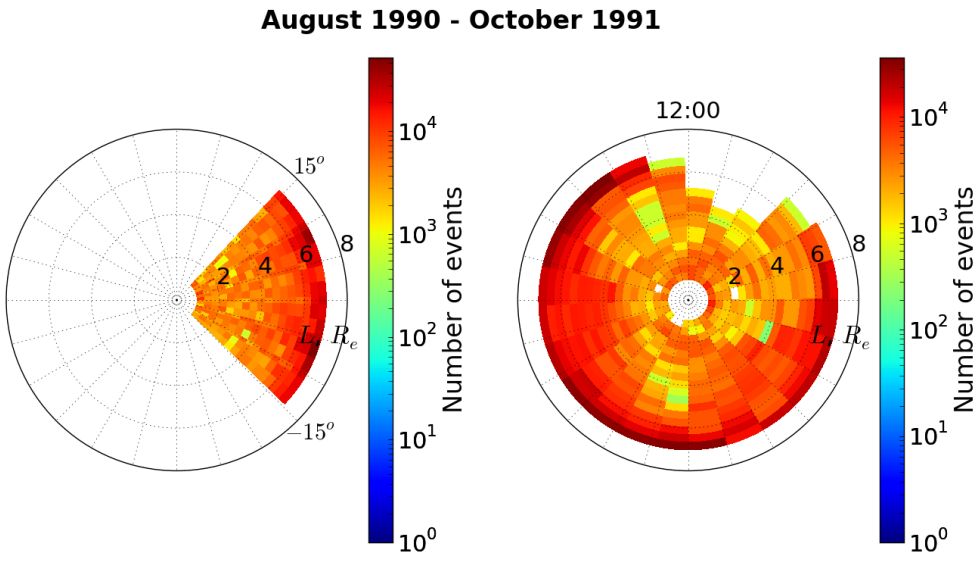

Figure 18: Orbital coverage of CRRES spacecraft during August 1990 - October 1991. The colour coding represents amount of measurements made by the spacecraft in a particular spatial sector.

6.2 CRRES data availability

Figure 18 shows orbital coverage of CRRES spacecraft during August 1990 - October 1991.

The data coverage available from CRRES, grouped according to K_p (low $0 \leq K_p < 3$, medium $3 \leq K_p < 5$ and high activity levels $K_p \geq 5$) is shown on figure 19. The colour coding represents number of measurements spacecraft made in a particular spatial sector during 1990-1991. The left-hand panel shows the orbital coverage in L-shell/λ coordinates which is obtained by summation over all MLT values, while the right-hand panel represents the coverage in L-shell/MLT coordinates obtained by summation over all latitudes along particular L-shell. During quiet geomagnetic conditions $K_p < 3$ the data coverage contains sufficient number of measurement points for performing statistical study only at the nightside of the magnetosphere. But the dayside data coverage does not contain enough measurement points. Since disturbed conditions occurred rarely during operation time of CRRES spacecraft the data coverage is very poor for $K_p > 3$.

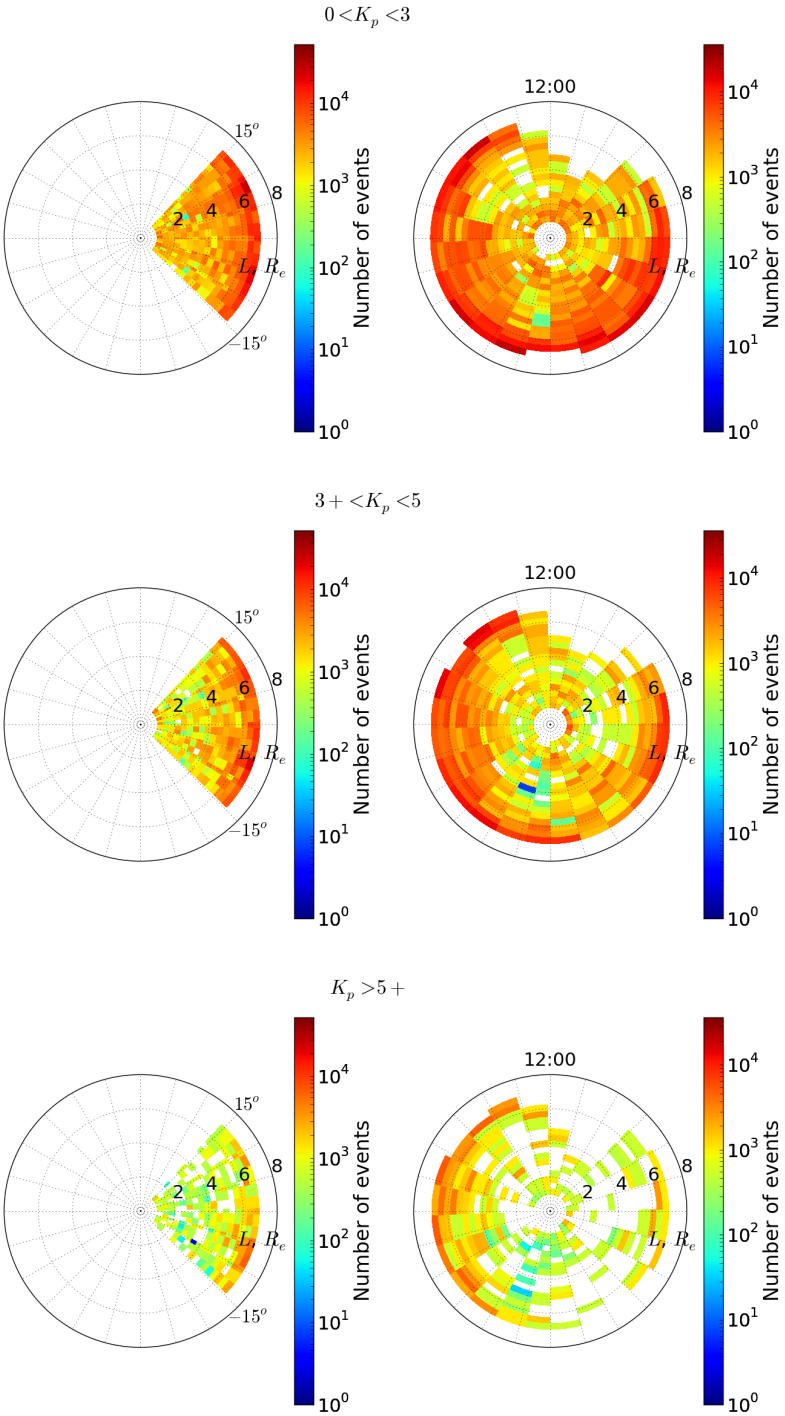

Figure 19: The orbital coverage of CRRES spacecraft during August 1990 - October 1991 corresponding to different levels of geomagnetic activity. The colour coding represents amount of measurements made by the spacecraft in a particular spatial sector.

Column	Units	From	To	Description
L		0.95	7	L-shell value
λ	degrees	-15	15	Magnetic latitude
MLT	hour	0	24	Magnetic local time
Epoch	date	19/08/1990	11/10/1991	Date and time
FR	V^2/m^2Hz	10^{-9}	1	Electric field intensity
Frequency	Hz	104	$4 \cdot 10^5$	Frequency for 128 channels of SFR
KP		0	100	Planetary K_p index
DST				Disturbance storm time index

Table 12: Description of CRRES .cdf file.

6.3 CRRES database description

Database consists of three files, each file contains wave events of particular type registered onboard of spacecraft. *crres_msw_pwe.dat*, *crres_hiss_pwe.dat* and *crres_lbc_pwe.dat* files contain magnetosonic, hiss and lower band chorus events respectively. The database contains measurements of SFR instrument of CRRES spacecraft from August 1990 to October 1991. File contain several columns which describe spacecraft position, time, geomagnetic activity and amplitude of corresponding emission. Table 12 gives description of available columns in .cdf file.

The dataset was formed on the basis of CDAWeb data. Signals with intensity less than 10^{-9} nT^2/Hz were interpreted as noise and were extracted from original dataset. We separate the entire dataset into 96 frequency channels logarithmically spaced in the frequency range from 24 Hz to 12.5 kHz. Each frequency channel was then scanned in order to eliminate all intervals with anomalously high magnitudes of spectral density. On average about 20% of the data has been thrown away during this quality check process.

7 VLF/ELF wave properties statistics in the Earth magnetosphere

Discrete ELF/VLF chorus emissions, the most intense electromagnetic plasma waves observed in the Earth's radiation belts and outer magnetosphere, have received increased attention in the past several years. Characterised by rising and falling tones in the frequency range from a few hundreds to several thousands of hertz (e.g., reviews by (Hayakawa *et al.*, 1990; Omura *et al.*, 1991; Sazhin and Hayakawa, 1992)), these emissions play the significant role in local acceleration of energetic electrons in the outer radiation belts (Horne *et al.*, 2005). Chorus is a burst-like wave emission observed in the near-Earth magnetosphere outside the plasmapause. These emissions are most often observed on the Earth's dawn side between 23:00 and 13:00 MLT (Meredith *et al.*, 2001, 2003; Tsurutani and Smith, 1974). Chorus emissions, which propagate in the whistler mode, usually consist of two narrow frequency range bands centered around one-half the electron gyrofrequency at the geomagnetic equator (f_{ce}) of the magnetic field line on which the waves are observed (Tsurutani and Smith, 1974). If present, the upper band exists in the frequency range of $f/f_{ce} \approx 0.5 - 0.75$ and contains discrete chorus elements rising at a few kHz/s. The lower band exists in the frequency range of $f/f_{ce} \approx 0.2 - 0.45$ and contains both elements rising at a few kHz/s and diffuse elements.

A number of ELF/VLF chorus emissions have been observed near the magnetic equatorial plane in the dayside outer magnetosphere. Wave normal vector directions of chorus in the outer magnetosphere were determined for the first time from data obtained with the OGO5 search coil magnetometer (Burton and Holzer, 1974). In (Hayakawa *et al.*, 1990) the GEOS l satellite wave data have been used to determine the wave normal directions of chorus emissions at geomagnetic latitudes near 17°, (L-shell about 7.6). Analysis of the wave normal and Poynting vectors for each element of the emissions has shown that these emissions are generated in the geomagnetic equator and propagate to higher latitudes in a non-ducted whistler mode (Burton and Holzer, 1974; Hayakawa *et al.*, 1990; Inan *et al.*,

2004; Yagitani *et al.*, 1999). The GEOTAIL spacecraft has observed many ELF/VLF chorus emissions in the Earth's outer magnetosphere with the Plasma Wave Instrument (PWI) (Nagano *et al.*, 1996).

In the inner and middle magnetosphere the onset of wave generation has been associated with substorm electron injections (Goldstein and Tsurutani, 1984). The source of the waves in the outer dayside region within a few R_E of the magnetopause is less well understood. In the radiation belts, chorus is believed to be generated through electron cyclotron instability by anisotropic distributions of energetic electrons in the 5 to 150 keV range. In the outer magnetosphere simultaneously measured wave and particle data registered onboard the GEOTAIL spacecraft for chorus emissions in the dayside outer magnetosphere were analysed in (Yagitani *et al.*, 1999). The anisotropy observed onboard GEOTAIL was too small to generate the observed chorus emissions by the linear cyclotron resonance mechanism. The co-existence of hiss and chorus has been observed frequently by satellites in the outer magnetosphere (Hattori *et al.*, 1991). A mechanism for hiss- triggered chorus based on GEOS-1 observations was proposed by (Hattori *et al.*, 1991).

The size of the generation region can be used to investigate and choose the generation mechanism. Before the Cluster mission, observations of ELF/VLF chorus emissions were carried out mainly by single spacecraft (Trakhtengerts, 1999). Considerable simultaneous chorus data were collected by ISEE1 and ISEE2 spacecraft (Gurnett *et al.*, 1979). Although the correlation scale based on comparison of spectrograms from ISEE1 and ISEE2 was estimated to be in the range of units of hundred kilometres.

Recent Poynting flux and polarization measurements on board the Cluster spacecraft confirmed not only that the chorus source is located close to the equatorial plane (Parrot *et al.*, 2003; Santolik and Gurnett, 2003; Santolík *et al.*, 2005) but also that the dimension of the chorus source region measured along the magnetic field lines is 3000-5000 km (Santolik and Gurnett, 2003). The radiation belt chorus generation region scales

were estimated theoretically (Helliwell, 1966; Trakhtengerts, 1999) and experimentally (Breneman *et al.*, 2009; Santolik and Gurnett, 2003) using data from coordinated Cluster observations. The problem is to determine the source size given the signal distortion due to whistler wave propagation through the random irregularities of the medium. (Santolik and Gurnett, 2003) and (Breneman *et al.*, 2009) determined the correlation lengths of chorus-type whistler waves based on multi-point Cluster WBD measurements near the chorus source region during the magnetic storm of 18 April 2002. Correlation scales were obtained from the dependence of the chorus wave amplitude correlation coefficient on the distance between Cluster spacecraft. Correlation was found to be significant throughout a range of separation distances 60-260 km parallel to and 7-100 km perpendicular to the background magnetic field line. At these scales, the correlation coefficient depends weakly on parallel separation and decreases with perpendicular separation. It varies between approximately 60 and 120 km for different data intervals. The spatial scales obtained were explained by a chorus generation region transverse to the spatial scales of the background magnetic field (Santolik and Gurnett, 2003).

The objective of this study is a reconstruction of the chorus emissions distribution in the radiation belts and in the inner magnetosphere. To achieve this aim the data from the electric and magnetic field measurements registered by EDC and SCM instruments onboard THEMIS spacecraft is used to determine averaged amplitude of the chorus signal around the equator region and its time coherency scale.

The distribution of the THEMIS EDC and SCM measurements during 2008-2014 in dependence on K_p index is shown in the figure 20. Chorus waves demonstrate very strong dependence on the magnetosphere activity. The increasing of the electric and magnetic amplitude of whistler waves with the K_p index is clearly seen from the figure for L-shell interval $L \in [4, 7]$. While for outer regions $L > 7$ the dependence is not obvious.

The occurrence rate of whistler waves in chorus frequency range for L-shell/MLT and L-shell/λ frames is shown in Figures 21a and 21d respectively. Occurrence rate is calcu-

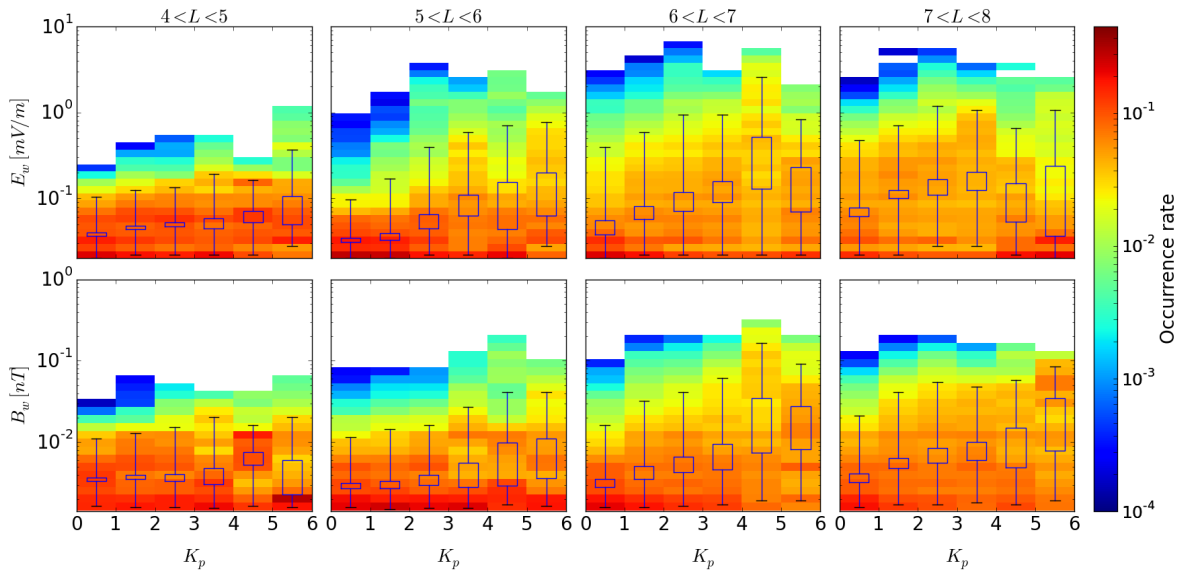

Figure 20: Distribution of whistler electric (top) and magnetic field (bottom) amplitudes as a function of K_p for ranges of L-shell. Blue boxes indicate intervals within first and third quartiles of the data. The input dataset is the average power in E (mV/m) and mean amplitude in B (nT). Dashed vertical bars indicate 0.05 and 0.95 cumulative levels. Figure is obtained using measurements registered on board THEMIS A spacecraft during 2008-2014.

lated as the ratio of number of measurements of whistler waves with magnetic component greater 4 pT on the total number of measurements in each bin. Whistler waves are distributed over a broad MLT range from the midnight through dawn to dusk sector (01:00-20:00 MLT). Note that the occurrence rate of whistler waves on the dayside is significantly higher that that on the nightside that is consistent with Li *et al.* (2011). However, two regions with high occurrence rate of whistler waves can be distinguished. One at L-shells $4 < L < 6$, where whistler waves are mainly observed at 05:00-20:00 MLT and another at L-shells $6 < L < 8$, where whistler waves are observed at 00:00-15:00 MLT. The average amplitude distribution of electric and magnetic components of whistler waves are shown in Figures 21b and 21c in L-shell/MLT frame. There is a general agreement between the occurrence distribution of electric and magnetic field measurements of whistler emissions. The typical magnetic component amplitude of whistler waves is greater 10 pT over the entire region that extends from pre-midnight to the pre-noon sector (22:00-11:00 MLT)

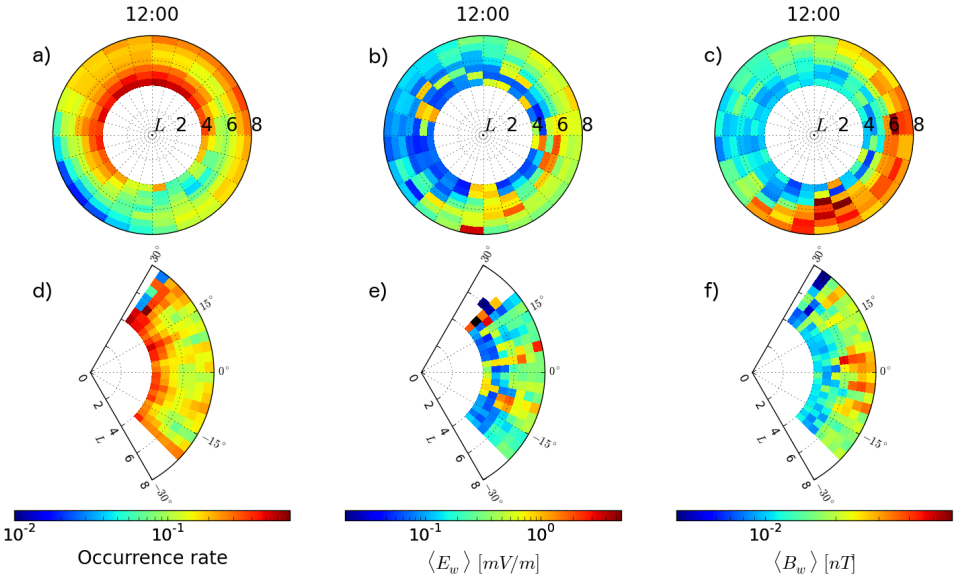

Figure 21: Occurrence rate of whistler waves shown in (a) L-shell/MLT and (d) L-shell/λ frames. Distributions of whistler averaged (b and e) electric and (c and f) magnetic wave amplitudes in L-shell/MLT and L-shell/λ frames. Figure is obtained using measurements registered on board THEMIS A spacecraft during 2008-2014.

with the maximum at $6 < L < 8$. In the dusk sector (15:00-20:00 MLT) the magnetic component amplitude is lower than that observed in the morning sector by almost an order of magnitude while the lowest intensity waves are observed in range 18:00-21:00 MLT at $4 < L < 6$.

The distribution is in a good agreement with previous studies (Meredith *et al.*, 2003) based on CRRES measurements, (Pokhotelov *et al.*, 2008) based on Cluster measurements (2001-2004) and the report by Agapitov 2008 based on Polar PWI measurements (1996-1997).

8 The chorus wave coherency scale

At current state there are already more than 5000 passes through magnetosphere in wide variety of L-shell and MLT values in equatorial plane since mission launch. Such amount of data can give us really good statistics of whistler waves in plasmasphere and radiation belts. As has already been pointed out, in order to successfully use the ERR methodology

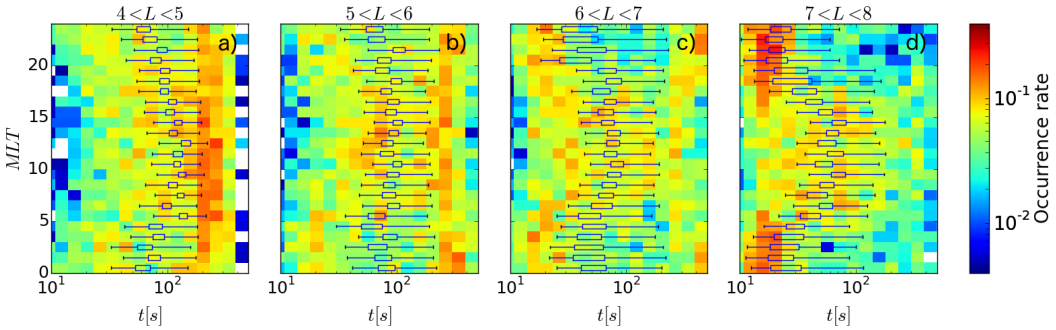

Figure 22: Whistler wave correlation time distribution at four different regions of the equatorial magnetosphere registered by THEMIS A during 2008-2014. Blue boxes indicate intervals within first and third quartiles of chorus correlation time. Horizontal bars indicate 0.05 and 0.95 cumulative levels.

a large number of independent 'output' data points are required. The goal was to find out minimum time scales at which measurements can be treated as independent, as well as its dependence on L-shell and MLT. To achieve this goal the whole equatorial cross-section of the inner magnetosphere $L \in [4, 8]$ was divided into a number of spatial bins defined as the volume in the equatorial region such that the radial size corresponds to 1 L-shell and an azimuthal width of 1 hour MLT. Total satellite path was divided on small tracks that belong to one of the bins and represent one satellite pass through the region.

We use autocorrelation value of the each track in order to determine if these tracks can be treated as independent measurements. The lower autocorrelation values of the signal is the more time series of the signal could be treated as independent and more independent measurements are available. However whistlers and magneto-sonic waves are highly coherent waves therefore tracks with low autocorrelation value contain less useful information about the waves under study. Therefore we use two different autocorrelation scales that correspond to noise and to the waves. The autocorrelation scales of the waves are used to determine if different tracks could be treated as independent measurements.

Autocorrelation analysis of FBK SCM measurements was performed for every track. Autocorrelation as a function of time shift was interpolated by Gauss function and Gauss dispersion was used as the estimation of correlation time.

Figure 22 show correlation time statistics for different MLT gathered during 2008-2014. Each panel represent correlation time distribution from four radial regions. Autocorrelation function typically exhibits two large peaks, one corresponding to time lag around 200 - 300 s and the other less than 100 s. The second correlation time maximum at ~ 300 s is clearly visible on panels b) and c). On panel a) the second maximum is less distinguishable and is completely absent on panel d). The existence of second maximum serves as evidence for two regimes of ELF/VLF emissions present in equatorial magnetosphere. The first regime is chorus wave emissions with characteristic correlation time $t_{corr} \sim 250$ s, and the second - low amplitude noise with $t_{corr} < 100$ s.

Figure 23a shows total correlation time statistics. Each line represents the correlation time distribution from measurements in separate radial bins. In order to investigate the occurrence of these peaks further a function consisting of two Gaussian curves (1) was fitted to correlation time distributions shown in Figure 23a using a non-linear least-squares fit:

$$f(x) = c_1 Gs(\mu_1, \sigma_1) + c_2 Gs(\mu_2, \sigma_2), \tag{1}$$

where Gs - Gaussian function, c_1, c_2 - height of the Gaussian function, μ_1, μ_2 - position of the centre of Gaussian function, σ_1, σ_2 - width of the "bell". We define characteristic correlation time scale of low intensity noise as $2\sigma_1$. The position of the second Gaussian function μ_2 is treated as the characteristic correlation time of high amplitude chorus emissions. The dependence of characteristic correlation time scales for the two kinds of ELF/VLF emissions on L-shell is shown on Figure 23b. The characteristic chorus emission and low amplitude noise correlation times are shown with blue and red dots respectively. The characteristic correlation time of chorus emissions tends to increase with L-shell from ~ 200 s at $L = 4$ to ~ 300 s at $L = 8$.

To understand the dependence of the correlation time on L-shell we explore whether injected electrons penetrating from the tail may be responsible and investigate whether the size of the active region may be proportional to the local gyroradius of energetic electrons:

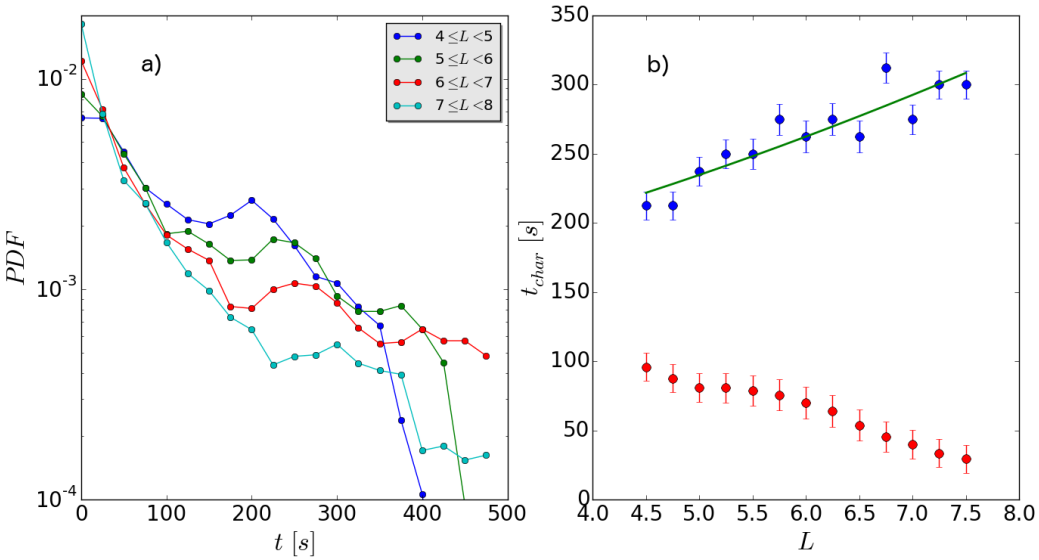

Figure 23: (a) Distribution of chorus wave correlation times at different radial distances of equatorial magnetosphere registered by THEMIS A during 2008-2014. Lines that correspond to different L-shell regions denoted by different colours. (b) Chorus emission characteristic correlation time dependency on L-shell. Chorus emission and low amplitude noise characteristic correlation times are shown with blue and red dots respectively. Green line denotes linear fitting of theoretical dependence of chorus correlation time on L-shell.

$r_g = v_\perp/\omega_{ce} = mv_\perp/eB$, where $v_\perp$ - velocity component perpendicular to magnetic field. Taking into account the conservation of the first adiabatic invariant $v_\perp^2/B = const$ during penetration of injected energetic electrons into inner magnetosphere from the tail and assuming a dipolar magnetic field we obtain: $r_g \sim 1/\sqrt{B} \sim L^{3/2}$. A linear fit to the chorus correlation time in Figure 23b leads to the following dependence: $t_{char} = 7.88L^{3/2} + 146.6$ (green line). Since the L-shell range studied here is rather narrow the approximate dependence describes the results shown in Figure 23b quite well. The observed dependence of the correlation time on L-shell presumably corresponds to the electrons gyroradius scales increase with L: the chorus active regions are related to the injected electrons penetrating from the tail, thus the size and temporal scales may be proportional to the characteristic scales of these particles (Agapitov *et al.*, 2010, 2011).

Estimated values of characteristic correlation time for chorus waves show us that individual satellite tracks that belong to one spatial bin can contain several uncorrelated occurrences of chorus events. Since the separation of the THEMIS A, D, and E exceeds the correlation length of the waves, data from all three satellites can be used to provide independent data points for ERR analysis. At the same time the separation of the Cluster spacecraft varied from a few kilometres to a few Re. Initially, we will consider data from a single spacecraft. However, if the number of points from the three THEMIS and one Cluster spacecraft is not sufficient to perform the ERR analysis we will consider using data from the other Cluster spacecraft provided that the intersatellite separation is not too small.

8.1 Conclusions

1. We collected data base of whistler waves observation in a vicinity of the geomagnetic equator (chorus generation region). It is found that vast amount of data is available to be analysed, comprehensively covering all MLT and L-shell in the range $L \in [2, 8]$ for a wide range of geomagnetic activity $K_p \in [0, 6]$.

2. Correlation time of chorus waves occurred during 2008-2014 was calculated. The decreasing of the chorus occurrence rate with the correlation time increasing can be seen. It was found that of characteristic correlation time decreases on chorus wave amplitude.

3. Potential number of THEMIS independent data points was estimated within each defined region to ensure that each region contains enough data points to enable a meaningful ERR analysis to be completed. It is found that separate orbit tracks that belong to particular spatial bin can contain several independent chorus wave measurements. Chorus wave events should be searched on smaller time intervals which can significantly increase number of data points per location.

4. Characteristic correlation time of chorus waves increases linearly on L-shell for wide range of $L \in [4, 7]$. It has to be taken into account as a criteria for breaking up some of the regions into smaller subregions to enable the possibility of investigating the relationship between wave amplitude and solar wind/geomagnetic parameters with a greater spatial resolution.

9 Cross calibration of satellite data

While data from all of the specified satellites has been added to the database and will be available to members of the scientific community it should be noted that not all data sets are directly comparable due to intercalibration issues. Currently only the Cluster and THEMIS datasets have been inter calibrated and are therefore directly comparable. This task was moderately straight forward since the instrument sensitivities as a function of frequency of the Cluster and THEMIS search coil magnetometers is fairly similar. However, this is not the case for the Polar, CRRES and DE instruments. More details regarding this issue may be found in the appendix.

10 Future Tasks

The completion of this task has provided the Project with sets of measurements of the wave amplitudes as functions of MLT, L-shell, magnetic latitude, Kp, and Dst from the satellites THEMIS A, D, and E, Cluster 4, Polar, CRRES, and DE-1. Due to cross calibration issues, the datasets from Polar, CRRES, and DE-1 require further analysis before they can be included within subsequent tasks. Hence future tasks will be based on the use of THEMIS and Cluster data alone. However, this should not be a problem as these are the two largest datasets that we planned to use.

These databases provide the basic data required for Task 4.3.

References

Agapitov, O., Krasnoselskikh, V., Zaliznyak, Y., Angelopoulos, V., Le Contel, O., and Rolland, G. (2010). Chorus source region localization in the Earth's outer magnetosphere using THEMIS measurements. *Annales Geophysicae*, **28**, 1377–1386.

Agapitov, O., Krasnoselskikh, V., Dudok de Wit, T., Khotyaintsev, Y., Pickett, J. S., Santolík, O., and Rolland, G. (2011). Multispacecraft observations of chorus emissions as a tool for the plasma density fluctuations' remote sensing. *Journal of Geophysical Research (Space Physics)*, **116**, 9222.

Agapitov, O., Artemyev, A., Krasnoselskikh, V., Khotyaintsev, Y. V., Mourenas, D., Breuillard, H., Balikhin, M., and Rolland, G. (2013). Statistics of whistler mode waves in the outer radiation belt: Cluster STAFF-SA measurements. *J. Geophys. Res.*, **118**(6), 3407–3420.

Anderson, R. R., Gurnett, D. A., and Odem, D. L. (1992). Crres plasma wave experiment. *Journal of Spacecraft and Rockets*, **29**(4), 570–573.

Auster, H., Glassmeier, K., Magnes, W., Aydogar, O., Baumjohann, W., Constantinescu,

D., Fischer, D., Fornacon, K., Georgescu, E., Harvey, P., *et al.* (2009). The THEMIS fluxgate magnetometer. In *The THEMIS Mission*, pages 235–264. Springer.

Bonnell, J., Mozer, F., Delory, G., Hull, A., Ergun, R., Cully, C., Angelopoulos, V., and Harvey, P. (2008). The electric field instrument (EFI) for THEMIS. *Space Sci. Rev.*, **141**(1-4), 303–341.

Breneman, A. W., Kletzing, C. A., Pickett, J., Chum, J., and Santolik, O. (2009). Statistics of multispacecraft observations of chorus dispersion and source location. *J. Geophys. Res.*, **114**(A6), 6202.

Burton, R. K. and Holzer, R. E. (1974). The origin and propagation of chorus in the outer magnetosphere. *J. Geophys. Res.*, **79**(7), 1014–1023.

Cornilleau-Wehrlin, N., Chauveau, P., Louis, S., Meyer, A., Nappa, J., Perraut, S., Rezeau, L., Robert, P., Roux, A., De Villedary, C., *et al.* (1997). The Cluster spatio-temporal analysis of field fluctuations (STAFF) experiment. In *The Cluster and Phoenix Missions*, pages 107–136. Springer.

Cornilleau-Wehrlin, N., Chanteur, G., Perraut, S., Rezeau, L., Robert, P., Roux, A., de Villedary, C., Canu, P., Maksimovic, M., de Conchy, Y., Lacombe, D. H. C., Lefeuvre, F., Parrot, M., Pinçon, J. L., Décréau, P. M. E., Harvey, C. C., Louarn, P., Santolik, O., Alleyne, H. S. C., Roth, M., Chust, T., Le Contel, O., and Staff Team (2003). First results obtained by the Cluster STAFF experiment. *Annales Geophysicae*, **21**, 437–456.

Credland, J., Mecke, G., and Ellwood, J. (1997). The Cluster mission: Esa's spacefleet to the magnetosphere. In *The Cluster and Phoenix Missions*, pages 33–64. Springer.

Cully, C., Bonnell, J., and Ergun, R. (2008). THEMIS observations of long-lived regions of large-amplitude whistler waves in the inner magnetosphere. *Geophys. Res. Lett.*, **35**(17).

Dunlop, M. W. (1990). Review of the Cluster orbit and separation strategy: Consequence for measurements. Technical report.

Escoubet, C., Fehringer, M., and Goldstein, M. (2001). Introduction the Cluster mission. In *Ann. Geofis.*, volume 19, pages 1197–1200.

Goldstein, B. E. and Tsurutani, B. T. (1984). Wave normal directions of chorus near the equatorial source region. *J. Geophys. Res.*, **89**(A5), 2789–2810.

Gurnett, D. and Inan, U. (1988). Plasma wave observations with the dynamics explorer 1 spacecraft. *Rev. Geophys.*, **26**(2), 285–316.

Gurnett, D. A., Anderson, R., Scarf, F., Fredricks, R., and Smith, E. (1979). Initial results from the ISEE-1 and-2 plasma wave investigation. *Space Sci. Rev.*, **23**(1), 103–122.

Hattori, K., Hayakawa, M., Lagoutte, D., Parrot, M., and Lefeuvre, F. (1991). Further evidence of triggering chorus emissions from wavelets in the hiss band. *Planet. Space Sci.*, **39**(11), 1465–1472.

Hayakawa, M., Hattori, K., Shimakura, S., Parrot, M., and Lefeuvre, F. (1990). Direction finding of chorus emissions in the outer magnetosphere and their generation and propagation. *Planet. Space Sci.*, **38**(1), 135–143.

Helliwell, R. A. (1966). Whistlers and related ionospheric phenomena. *Geophysical Journal*, **11**(1), 563–564.

Horne, R. B., Thorne, R. M., Glauert, S. A., Albert, J. M., Meredith, N. P., and Anderson, R. R. (2005). Timescale for radiation belt electron acceleration by whistler mode chorus waves. *J. Geophys. Res.*, **110**(A3).

Horne, R. B., Kersten, T., Glauert, S. A., Meredith, N. P., Boscher, D., Sicard-Piet, A., Thorne, R. M., and Li, W. (2013). A new diffusion matrix for whistler mode chorus waves. *J. Geophys. Res.*, **118**(10), 6302–6318.

Inan, U. S., Platino, M., Bell, T. F., Gurnett, D., and Pickett, J. (2004). Cluster measurements of rapidly moving sources of ELF/VLF chorus. *J. Geophys. Res.*, **109**(A5).

Li, W., Bortnik, J., Thorne, R. M., and Angelopoulos, V. (2011). Global distribution of wave amplitudes and wave normal angles of chorus waves using THEMIS wave observations. *Journal of Geophysical Research (Space Physics)*, **116**(A15), 12 205.

Meredith, N. P., Horne, R. B., and Anderson, R. R. (2001). Substorm dependence of chorus amplitudes: Implications for the acceleration of electrons to relativistic energies. *J. Geophys. Res.*, **106**, 13 165–13 178.

Meredith, N. P., Horne, R. B., Thorne, R. M., and Anderson, R. R. (2003). Favored regions for chorus-driven electron acceleration to relativistic energies in the earth's outer radiation belt. *Geophys. Res. Lett.*, **30**(16), 1871.

Meredith, N. P., Horne, R. B., Sicard-Piet, A., Boscher, D., Yearby, K. H., Li, W., and Thorne, R. M. (2012). Global model of lower band and upper band chorus from multiple satellite observations. *J. Geophys. Res.*, **117**(A10).

Nagano, I., Yagitani, S., Kojima, H., and Matsumoto, H. (1996). Analysis of wave normal and poynting vectors of the chorus emissions observed by geotail. *Journal of geomagnetism and geoelectricity*, **48**(3), 299–307.

Omura, Y., Nunn, D., Matsumoto, H., and Rycroft, M. (1991). A review of observational, theoretical and numerical studies of VLF triggered emissions. **53**, 351–368.

Parrot, M., Santolik, O., Cornilleau-Wehrlin, N., Maksimovic, M., and Harvey, C. (2003). Source location of chorus emissions observed by Cluster. *Ann. Geofis.*, **21**(2), 473–480.

Pokhotelov, D., Lefeuvre, F., Horne, R. B., and Cornilleau-Wehrlin, N. (2008). Survey of ELF-VLF plasma waves in outer radiation belt observed by Cluster STAFF-SA experiment. *Ann. Geofis.*, **26**(11), 3269–3277.

Reeves, G., Spence, H., Henderson, M., Morley, S., Friedel, R., Funsten, H., Baker, D., Kanekal, S., Blake, J., Fennell, J., Claudepierre, S., Thorne, R., Turner, D., Kletzing, C., Kurth, W., Larsen, B., and Niehof, J. (2013). Electron acceleration in the heart of the Van Allen radiation belts. *Science*, **341**, 991–994. ISSN 1095-9203.

Roux, A., Le Contel, O., Coillot, C., Bouabdellah, A., De La Porte, B., Alison, D., Ruocco, S., and Vassal, M.-C. (2009). The search coil magnetometer for THEMIS. In *The THEMIS Mission*, pages 265–275. Springer.

Santolik, O. and Gurnett, D. (2003). Transverse dimensions of chorus in the source region. *Geophys. Res. Lett.*, **30**(2), 1031.

Santolík, O., Gurnett, D., Pickett, J., Parrot, M., and Cornilleau-Wehrlin, N. (2005). Central position of the source region of storm-time chorus. *Planet. Space Sci.*, **53**(1), 299–305.

Sazhin, S. and Hayakawa, M. (1992). Magnetospheric chorus emissions: A review. *Planet. Space Sci.*, **40**(5), 681–697.

Thorne, R. M. (2010). Radiation belt dynamics: The importance of wave-particle interactions. *Geophys. Res. Lett.*, **33**(22), 22 107.

Trakhtengerts, V. Y. (1999). A generation mechanism for chorus emission. *Ann. Geofis.*, **17**(1), 95–100.

Tsurutani, B. T. and Smith, E. J. (1974). Postmidnight chorus: A substorm phenomenon. *J. Geophys. Res.*, **79**(1), 118–127.

Tsurutani, B. T. and Smith, E. J. (1977). Two types of magnetospheric elf chorus and their substorm dependences. *J. Geophys. Res.*, **82**(32), 5112–5128.

Yagitani, S., Nagano, I., Matsumoto, H., Omura, Y., Paterson, W., Frank, L., and Anderson, R. (1999). Wave and particle measurements for chorus emissions by GEOTAIL in the magnetosphere. *Adv. Space Res.*, **24**(1), 91–94.

A Intercalibration

Magnetic field variations in the frequency range from several Hz to several kHz are measured by inductive type search coil magnetometers (SCM). The Search Coil Magnetometer unit SCM is an inductive magnetic sensor. It is made of a core in a high permeability material (ferrite or permalloy) on which are wound a main coil with several thousand turns and a secondary coil with a few turns. The induced voltage in the main coil is:

$$e = \mu_{eff} \cdot N \cdot S \cdot \frac{d}{dt} < B > \tag{2}$$

Where μ_{eff} is the relative effective permeability, N the number of wire turns, S the cross section of the core, B the magnetic induction outside the core, aligned with the core. μ_{eff} depends strongly on the ratio L/d (length / diameter) of the core, and on the permeability of the core.

The secondary coil is used to create a flux feedback in order to have a flat frequency response on a bandwidth centered on the resonance frequency of the main coil. The induced voltage is raised to a proper level by a preamplifier to allow its transportation to the analyzers.

A.1 Hardware description

The triaxial sensor is a search coil magnetometer composed of 3 orthogonal search coil antennas assembled in the most compact way as possible by the body of the sensor. An important characteristic of the instrument is its sensitivity. Typically, this type of instrument covers four decades in the frequency domain, and its characteristics are strongly dependent upon its resonance frequency, which corresponds to the frequency at which the instrument is most sensitive. The sensitivity curve (Figure 24) has some similar quasi-parabolic shape for most of instruments of such a type.

This figure, adapted from Cornilleau-Wehrlin et al., (2003) represents the STAFF instrument sensitivity curve, and an important characteristics here is that the best sensitivity for this instrument as well as similar instrument onboard THEMIS spacecraft

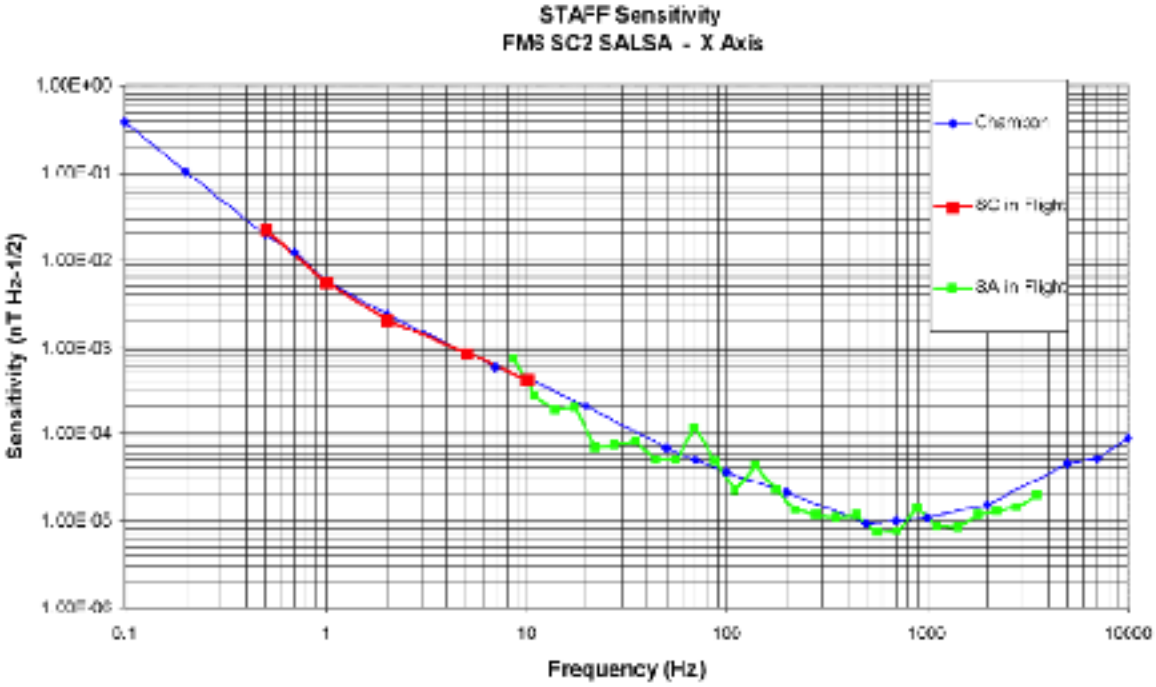

Figure 24: Sensitivity curve of the Cluster STAFF search coil magnetometer..

is around 600-800 Hz. This implies that it well adapted for the studies of signals in the frequency range from 100 Hz to 4 kHz, the range of signals under investigation in our studies. The search coil magnetometers onboard Polar and DE1, provided by the University of Iowa, have quite different characteristics. The resonance frequency of the PWI search coil magnetometer (http://pwg.gsfc.nasa.gov/istp/polar/polar_inst.html#PWI) indicates that it's resonance frequency (and similarly of the instrument onboard DE 1) is equal to 10 kHz, and the best sensitivity at this frequency is of the same order as on the curve of STAFF instrument. This results in the deterioration of the sensitivity and also a higher level of noise of the instrument in the frequency range of interest for our studies. Thus the procedure for the selection of the signals to be included into the statistical studies as well as amplitude characterisation should use the criteria quite different from those for Cluster and THEMIS missions. We are currently working on the procedures for inter-calibration between the data of these missions, but this work is not completed.